Photonic band gap templating using optical interference lithography

Timothy Y. M. Chan, Ovidiu Toader, and Sajeev John
Department of Physics, University of Toronto, 60 St. George Street, Toronto, Ontario, M5S 1A7, Canada
(Received 23 June 2004; published 7 April 2005)

We describe the properties of three families of inversion-symmetric, large photonic band-gap (PBG) template architectures defined by iso-intensity surfaces in four beam laser interference patterns. These templates can be fabricated by optical interference (holographic) lithography in a suitable polymer photo-resist. PBG materials can be synthesized from these templates using two stages of infiltration and inversion, first with silica and second with silicon. By considering point and space group symmetries to produce laser interference patterns with the smallest possible irreducible Brillouin zones, we obtain laser beam intensities, directions, and polarizations which generate a diamond-like (fcc) crystal, a novel body-centered cubic (bcc) architecture, and a simple-cubic (sc) structure. We obtain laser beam parameters that maximize the intensity contrasts of the interference patterns. This optimizes the robustness of the holographic lithography to inhomogeneity in the polymer photo-resist. When the optimized iso-intensity surface defines a silicon to air boundary (dielectric contrast of 11.9 to 1), the fcc, bcc, and sc crystals have PBG to center frequency ratios of 25%, 21%, and 11%, respectively. A full PBG forms for the diamond-like crystal when the refractive index contrast exceeds 1.97 to 1. We illustrate a noninversion symmetric PBG architecture that interpolates between a simple fcc structure and a diamond network structure. This crystal exhibits two distinct and complete photonic band gaps. We also describe a generalized class of tetragonal photonic crystals that interpolate between and extrapolate beyond the diamond-like crystal and the optimized bcc crystal. We demonstrate the extent to which the resulting PBG materials are robust against perturbations to the laser beam amplitudes and polarizations, and template inhomogeneity. The body centered cubic structure exhibits the maximum robustness overall.

DOI: 10.1103/PhysRevE.71.046605 PACS number(s): 42.70.Qs

I. INTRODUCTION

Photonic band-gap (PBG) materials [1,2] are periodically ordered dielectric microstructures that facilitate the localization of light [3]. This is a new frontier in quantum electrodynamics [4], and provides a robust platform for integrating active and passive devices in an all-optical micro-chip [5]. For example, by introducing line defects into the periodic dielectric structure of the PBG material, it is possible to guide light through micron-scale, single-mode air-waveguide channels with sharp, low-loss bends [6–8]. PBG materials can also facilitate frequency selective control over spontaneous emission of light from individual atoms in the circuit, through control of the local electromagnetic density of states. As a result, active devices such as zero threshold lasers [9] and, possibly, all-optical transistors [10] may be included on-chip. In order to realize the goal of a photonic band gap material-based optical microchip, it is necessary to have high quality, three-dimensional (3D) PBG materials. The design and efficient, low-cost micro-fabrication of such materials have been a major scientific challenge over the past decade. Novel experimental methods for templating, inversion, and replication [11,12] have made this paramount goal a near term reality. The optical properties of PBG materials scale with their lattice constants. PBG materials destined for use in optical telecommunications circuits must have submicron lattice constants. At the same time, the practical benefits of a PBG material-based optical circuit necessitate low-cost manufacturing of such materials with long range order (LRO) on the scale of hundreds of lattice constants. Optical interference lithography [13–15] provides a unique opportunity to satisfy both requirements while maintaining a high degree of flexibility in the detailed PBG architecture.

Early considerations of the photonic band structure focused on the face centered cubic (fcc) lattice because the first Brillouin zone (BZ) of this lattice exhibits the least anisotropy. In other words, the difference between the shortest and longest distances from the center to the surface of the first BZ is the smallest. This, it was reasoned [1,2], increased the likelihood that one-dimensional stop-gaps in all directions would overlap and produce a 3D PBG. It was shown [16], however, that a spherical scatterer within the fcc unit (Wigner-Seitz) cell prevents the creation of a PBG between the lowest possible bands due to the polarization degree of freedom of the electromagnetic field. The diamond structure, which can be viewed as an fcc lattice with a two "atom" basis, breaks this spherical symmetry while retaining the fcc BZ. Indeed, a diamond lattice of overlapping air spheres was theoretically shown in [16] to possess a sizeable 3D PBG, approximately 27% of the center frequency when the air spheres are in a background material with a dielectric constant of 11.9, corresponding to Si.

Although the diamond lattice has proven difficult to fabricate on the micron scale, the possibility of a large PBG has led to several theoretical blueprints and subsequent fabrication attempts for photonic crystals based on "diamond-like" structures which employ nonspherical bases on an fcc lattice. This began with the fabrication [17] of an fcc lattice of crisscrossing pores exhibiting a 3D PBG in the microwave spectrum. The straightforward but tedious fabrication on the centimeter scale has spurred many attempts to replicate this structure on the submicron scale as required for a PBG in the optical regime. However, this has proven to be very challenging. Methods involving electron beam lithography fol-

lowed by reactive ion etching [18,19] were successful in producing submicron pores, but the resulting slabs were only a few periods thick and severe imperfections occurred at the pore crossing points. Experiments with deep x-ray lithography (LIGA) patterning of an x-ray sensitive resist [20] have produced several periods of the criss-crossing pores, even allowing for the incorporation of controlled defects by multiple exposures [21]. However, structures patterned in this fashion, to date, have lattice constants which are too large for a PBG in the optical regime. A similar outcome has been reported using a hybrid scheme involving photo-electrochemical etching followed by focused ion beam etching in macroporous silicon. This method was used to synthesize a five-periods thick slab with a photonic band gap centered around 3μm [22]. Photo-electrochemical etching methods alone [23] have also been used to produce an elongated version of the fcc lattice of criss-crossing pores [24] with high aspect ratios, but as a result of the elongation, the photonic band gap is reduced in size [25]. Recently, new "slanted pore" architectures have been introduced [26] whose simpler geometries may facilitate their fabrication by various pore etching methods.

Another diamond-like structure is the layer-by-layer "woodpile" architecture consisting of stacked two-dimensional photonic crystals [27,28]. There have been several approaches to address the fabrication of woodpile architectures, but no large scale (with more than three unit cells normal to the substrate) woodpile photonic crystals operating at optical frequencies have been mass-produced as yet. The use of established silicon micromachining techniques such as repetitive deposition and etching have produced high-quality structures with relevant feature sizes, but the structures are only about one period (between two and five layers) thick [29,30]. Similarly, experiments using wafer-fusion and laser-assisted alignment [31] produced only two to three periods of the woodpile in the third dimension. An inexpensive but tedious method involving nanofabrication of two-dimensional layers followed by microassembly of the separate layers [32] provides a simple way to introduce defects into the woodpile structure because each layer can be fabricated uniquely. Unfortunately only up to four layers have been assembled so far. On the other hand, woodpiles synthesized by laser-induced chemical vapor deposition [33] are limited only in the number of layers by the size of the deposition chamber, but due to the laser spot size, the resulting PBG is centered around 75 μm. Recently, "direct laser writing" processes involving two-photon absorption (causing polymerization) in resins have been used to produce woodpile structures as a proof of concept [34,35].

An alternative PBG design, suitable for large-scale microfabrication, is an architecture involving glancing angle deposition methods [36] leading to the formation of silicon square spiral posts onto a silicon substrate. For suitably architectured spiral posts, a PBG as large as 24% of the gap center frequency has been predicted [37,38]. Optical reflectivity in a weakly disordered version of these silicon square spiral crystals has revealed a 3D PBG of roughly 10% relative to the center frequency [39].

While diamond and diamond-like structures may exhibit large PBGs, difficulties in fabrication have led to the consideration of other blueprints which sacrifice theoretical gap size in favor of feasibility of large-scale synthesis. One such blueprint is the fcc lattice of close-packed spheres (opal lattice), which does not have a PBG between the lowest possible bands, but does have a small PBG between the higher bands [40]. Moreover, the concept of fabricating opal structures by colloidal self-assembly has a long established history [41,42]. However, the materials suitable for the self-assembly process do not have large dielectric constants and low absorption at optical frequencies. Instead, self-assembled silica spheres are used as a template which is inverted by chemical vapor deposition of silicon, followed by selective etching of the template [11,43,44]. This process can now be performed at large scales. It has been shown [45] that by only partially infiltrating the template with silicon, a structure with a PBG of nearly 9% of the gap center frequency can be obtained. However, the small PBG of the inverted opal structure is fragile and vulnerable to disorder [46], requiring that fabrication methods must yield very high quality structures.

Many previous attempts to synthesize PBG materials have struggled to adapt various fabrication methods to emulate theoretical blueprints ill suited to fabrication at submicron length scales. Other attempts have focused on theoretically adjusting the fabrication parameters of a well-established technique in search of a PBG. The optical interference lithography method, described in this paper, offers a unique opportunity for efficient large-scale micro-fabrication of 3D PBG structures with large gaps in the optical regime. By employing the 3D interference pattern of four or more laser beams to expose a photopolymerizable material such as a photo-resist or polymerizable resin [13–15,47–52], nearly perfect LRO can be maintained over length scales much larger than the lattice constant of the photonic crystal (PC). At the same time, this technique allows straightforward control over the periodic properties (Fourier coefficients) of the resulting structure through the laser beam parameters. The photo-resist material undergoes a chemical alteration when the total light intensity due to the interference pattern, $I(\vec{r})$, at position $\vec{r}$, is maintained over a time interval $\delta\tau$ such that the "exposure" $I(\vec{r})\delta\tau$ exceeds a specified threshold, T. For a negative photo-resist, the "underexposed" region can be selectively removed using a developer substance which leaves the "overexposed" regions intact. (For a positive photo-resist, overexposed regions are removed, leaving the underexposed regions intact.) The developed photo-resist can then be infiltrated at room temperature with SiO_2 [12] and burned away, leaving behind a daughter "inverse" template. Finally, the daughter template is inverted by high temperature infiltration with silicon [11,53] and selective chemical etching of the SiO_2. As a result, a 3D silicon PC is formed, in which the silicon-air boundary is defined by the original, optical, isointensity surface $I(\vec{r})\delta\tau = T$. Alternatively, the photo-resist template can be infiltrated with a high refractive index material such as CdSe [54], which results in an inverted PC after the photo-resist is burned or chemically etched away. A third option is to use a photopolymerizable film which contains titanium [55], producing a direct PC after exposure to an intensity pattern and removal of underexposed material.

In this paper, we discuss the formation of 3D PCs using holographic lithography based on the interference of four

laser beams. Other proposed configurations include the use of multiple exposures and phase shifts between exposures [56,57] and a hybrid five beam configuration with three beams forming a two-dimensional pattern and two other beams forming a one-dimensional pattern [15] in the out of plane direction. However, these configurations require careful manipulation of the relative phases between beams and between exposures. In contrast, in a four beam, single exposure configuration, the relative phases between laser beams does not change the shape of the the interference pattern. In previous theoretical reports, four beam holographic lithography configurations were used [56,58,59] to create structures which emulate particular cases of triply periodic minimal surfaces [60], which have been shown [61,62] to produce large 3D PBGs. The resulting PCs included a diamond-like structure, a "gyroid" structure with body-centered cubic (bcc) Bravais lattice symmetry, and a simple cubic (sc) structure. Using simpler symmetry arguments, holographic beam configurations for the diamond-like structure and a novel bcc structure have been derived [63]. Here, we describe our approach in detail and find alternative beam configurations for producing the diamond-like, bcc, and sc structures in which the intensity contrast is maximized. We also explore the robustness of the resulting PBGs against perturbations in the beam polarizations and amplitudes. Both the diamond and bcc structures are robust against deviations in the experimental control parameters.

In Sec. II we introduce our framework for describing structures created by holographic lithography. Section III presents our design process for achieving 3D photonic crystals using this method, using the three cubic Bravais lattices. Section IV describes a generalized class of tetragonal PBG materials that encompass both the diamond network and bcc structures. Section V describes the properties of our holographic photonic crystals relevant to robust micro-fabrication and error-tolerant PBG formation.

II. STRUCTURE DESCRIPTION

The interference of N monochromatic plane waves of frequency ω, wave vectors $\vec{G}_i$, polarization vectors $\vec{\epsilon}_i$, phases θ_i, and real amplitudes $\mathcal{E}_i$ creates an electric field given by

$$\vec{E}(\vec{r},t) = e^{-i\omega t} e^{i(\vec{G}_0\cdot\vec{r}+\theta_0)} \left(\mathcal{E}_0\vec{\epsilon}_0 + \sum_{i=1}^{N-1} \mathcal{E}_i\vec{\epsilon}_i e^{i(\vec{K}_i\vec{r}+\gamma_i)} \right),$$

where

$$\vec{K}_i \equiv \vec{G}_i - \vec{G}_0 \tag{1}$$

and $\gamma_i \equiv \theta_i - \theta_0$. The corresponding, stationary intensity pattern is given by

$$I(\vec{r}) \equiv \vec{E}^*(\vec{r},t)\cdot\vec{E}(\vec{r},t) = \sum_{i=0}^{N-1} \mathcal{E}_i^2 + 2\sum_{i=1}^{N-1} \mathcal{E}_0\mathcal{E}_i|\vec{\epsilon}_0^*\cdot\vec{\epsilon}_i|\cos(\vec{K}_i\cdot\vec{r} + \gamma_i + \phi_i) + 2\sum_{i>j=1}^{N-1} \mathcal{E}_i\mathcal{E}_j|\vec{\epsilon}_i^*\cdot\vec{\epsilon}_j|\cos(\vec{K}_{ij}\cdot\vec{r} + \gamma_i - \gamma_j + \phi_{ij}), \tag{2}$$

where $\vec{K}_{ij} \equiv \vec{K}_i - \vec{K}_j$, $\phi_i \equiv \arg(\vec{\epsilon}_0^*\cdot\vec{\epsilon}_i)$, and $\phi_{ij} \equiv \arg(\vec{\epsilon}_i^*\cdot\vec{\epsilon}_j)$. The holographic structure is a two phase medium whose phase boundary is defined by the "shape" function

$$S(\vec{r}, I_{thr}^{expt}) = \Theta(I(\vec{r}) - I_{thr}^{expt}),$$

where I_{thr}^{expt} is a threshold value and $\Theta = 1$ for $x \geq 0$ and zero otherwise (Heaviside step function). By convention, we assume the high intensity regions in Eq. (2) become the silicon component of the photonic crystal [$\varepsilon(\vec{r}) = 1$ where $I(\vec{r}) < I_{thr}^{expt}$ and $\varepsilon(\vec{r}) = 11.9$ where $I(\vec{r}) \geq I_{thr}^{expt}$]. This corresponds to the case in which a negative photo-resist is used to make the photonic crystal template. It will be shown in Sec. V that for the optimized structures considered here, equivalent structures can be obtained with a positive photo-resist by simply adjusting the threshold I_{thr}^{expt}.

In the case $N=4$ (which provides the minimum number of non-collinear beams required to produce a nontrivial 3D intensity pattern), Eq. (2) becomes $I(\vec{r}) = I_0 + 2\Delta I(\vec{r})$, where $I_0 \equiv \mathcal{E}_0^2 + \mathcal{E}_1^2 + \mathcal{E}_2^2 + \mathcal{E}_3^2$and

$$\begin{aligned}\Delta I(\vec{r}) \equiv\ & c_1\cos(\vec{K}_1\cdot\vec{r} + \gamma_1 + \phi_1) + c_2\cos(\vec{K}_2\cdot\vec{r} + \gamma_2 + \phi_2) \\ & + c_3\cos(\vec{K}_3\cdot\vec{r} + \gamma_3 + \phi_3) + c_{12}\cos(\vec{K}_{12}\cdot\vec{r} + \gamma_1 - \gamma_2 \\ & + \phi_{12}) + c_{13}\cos(\vec{K}_{13}\cdot\vec{r} + \gamma_1 - \gamma_3 + \phi_{13}) \\ & + c_{23}\cos(\vec{K}_{23}\cdot\vec{r} + \gamma_2 - \gamma_3 + \phi_{23}),\end{aligned} \tag{3}$$

with

$$c_i = \mathcal{E}_0\mathcal{E}_i|\vec{\epsilon}_0^*\cdot\vec{\epsilon}_i|; c_{ij} = \mathcal{E}_i\mathcal{E}_j|\vec{\epsilon}_i^*\cdot\vec{\epsilon}_j|. \tag{4}$$

The spatial modulation of the intensity pattern given by Eq. (3) is periodic with a lattice whose primitive vectors, $\vec{a}_i$, satisfy $\vec{K}_i\cdot\vec{a}_j = 2\pi n\delta_{ij}$, where n is an integer. As a consequence, the lattice constants are inversely proportional to the frequency of the laser beams.

The phase factors γ_i in Eq. (3), which result from the relative phases of the laser beams, can be simultaneously eliminated by a translation of the origin by $\vec{\rho} = \gamma_1\vec{\eta}_1 + \gamma_2\vec{\eta}_2 + \gamma_3\vec{\eta}_3$, where $\vec{\eta}_i$ satisfy $\vec{K}_i\cdot\vec{\eta}_j = \delta_{ij}$. For configurations with more than four beams, the relative beam phases impart more than a simple translation in the intensity pattern, and cannot be easily ignored. On the other hand, the phase factors ϕ_i and ϕ_{ij}, arising from the dot products between beam polarization vectors, cannot in general be simultaneously eliminated. In the case of linearly polarized beams, ϕ_i and ϕ_{ij} are zero for all i and j and the intensity pattern is always inversion symmetric relative to position $\vec{\rho}$. However, in the case of elliptically polarized beams it is possible to obtain an interference pattern that is not inversion symmetric.

By rewriting the "experimental" intensity threshold as $I_{thr}^{expt} = I_0 + 2I_{thr}$ we arrive at the following simplified shape function:

$$\Theta(I(\vec{r}) - I_{thr}^{expt}) = \Theta(\Delta I(\vec{r}) - I_{thr}) \tag{5}$$

In what follows, we focus our discussion of the resulting shapes on the simplified intensity pattern in Eq. (3). [The intensity background I_0 is nevertheless important, as a large background intensity will overwhelm the variation $\Delta I(\vec{r})$.]

III. DESIGN OF HOLOGRAPHIC STRUCTURES WHICH EXHIBIT PHOTONIC BAND GAPS

We consider the design of holographic structures with inversion symmetry. A sufficient condition for this requirement to be fulfilled is that linearly polarized beams are used, or (in the case that elliptically polarized beams are used) that the phases ϕ_i and ϕ_{ij} vanish for all i and j. In this case, the design problem consists of identifying the set

$$\mathcal{C} = \{c_i, c_{ij}\}_{i<j=\overline{1,3}} \tag{6}$$

of six polarization and amplitude coefficients (some possibly 0), three $\vec{K}_i$ vectors, and suitable threshold I_{thr}, that generates a photonic crystal [through the shape function given by Eq. (5)] with a complete PBG. Given the parameters of the interference pattern $\mathcal{C}$ and $\vec{K}_i$, the laser beam directions, amplitudes, and polarizations are determined by

1. Finding the four beam directions, $\{\vec{G}_i\}_{i=\overline{0,3}}$, which satisfy Eq. (1).

2. Using $\vec{G}_i$ from stage 1 to find the four amplitudes and polarization vectors, $\{\boldsymbol{\mathcal{E}}_i, \vec{\epsilon}_i\}_{i=\overline{0,3}}$, which satisfy the nonlinear set of six equations given by Eq. (4).

The identification of $\mathcal{C}$ and the choice of $\vec{K}_i$ are obtained by two guiding principles: (*i*) choose a given Bravais lattice, and (*ii*) identify architectures leading to the smallest possible irreducible Brillouin zones (IBZ), then incrementally relax this condition if the resulting structure is too symmetric for a fundamental gap to open. In order to satisfy criterion (*i*), it is necessary and sufficient to choose the three $\vec{K}_i$ vectors to be linear combinations with **integral** coefficients of vectors from the set $\{\vec{b}_i\}$, where we denote by $\{\vec{a}_i, \vec{b}_i\}_{i=\overline{1,3}}$ a set of primitive and reciprocal vectors, respectively, of the desired Bravais lattice. On the other hand, criterion (*ii*) is far more restrictive. Indeed, only a very limited set of $\{\mathcal{C}, \vec{K}_i\}$ combinations generate intensity patterns with sufficiently high symmetry.

Suppose that the desired holographic structure has a cubic symmetry (sc, bcc, or fcc). Figure 1 shows several reciprocal lattice vectors of a simple cubic lattice, grouped by length. In order of increasing length, the first three sets of lattice vectors in the cubic reciprocal space are

- $\mathcal{B}^s = \{\pm\vec{b}_i^s\}$ of length $2\pi/a$, reaching the centers of the cube faces (red online),
- $\mathcal{B}^b = \{\pm\vec{b}_i^b\} \cup \{\vec{b}_i^b - \vec{b}_j^b\}_{i\neq j}$ of length $2\pi\sqrt{2}/a$, reaching the centers of the cube edges, (green online), and
- $\mathcal{B}^f = \{\pm\vec{b}_i^f\} \cup \{\pm(\vec{b}_1^f + \vec{b}_2^f + \vec{b}_3^f)\}$ of length $2\pi\sqrt{3}/a$, reaching the cube corners. (blue online)

i and j run from 1 to 3 and $\vec{b}_i^s$, $\vec{b}_i^b$, and $\vec{b}_i^f$ denote the three primitive vectors of the sc, bcc, and fcc reciprocal lattices, respectively.

Choosing $\vec{K}$ vectors from one of these sets generates a holographic structure with a specific cubic symmetry. The first order reciprocal lattice vectors generate an sc spatial lattice, the second order vectors a bcc lattice, and the third order vectors a fcc lattice. The fourth set of vectors (not shown in Fig. 1) again generates an sc lattice, with a lattice constant of $|a|/2$ in this case. Similarly, higher order sets generate intensity patterns that can be described as one of the fundamental lattices (sc, fcc, or bcc) with increasingly small lattice constants. We therefore restrict our choice for the set of target vectors to the first three, illustrated sets. We define the set $\mathcal{T}$ of "target vectors" as a subset $\mathcal{T} \subset \mathcal{K} \equiv \{\vec{K}_1, \vec{K}_2, \vec{K}_3, \vec{K}_{12}, \vec{K}_{13}, \vec{K}_{23}\}$ corresponding to nonzero terms in Eq. (3) (or, equivalently, nonzero coefficients in $\mathcal{C}$). Accordingly, we define $\mathcal{C}_\mathcal{T} \subset \mathcal{C}$ as the subset of nonzero coefficients of $\mathcal{C}$. The requirement of high symmetry can be achieved by choosing $\mathcal{T}$ simply to be a subset of one of the vector sets $\mathcal{B}^*$. Since $\Delta I(\vec{r})$ is insensitive to the sign of the target vectors in $\mathcal{T}$, an upper bound on the size of the sets $\mathcal{T}$ and $\mathcal{C}_\mathcal{T}$ is 3 in the case of $\mathcal{B}^s$, 6 in the case of $\mathcal{B}^b$, and 4 in the case of $\mathcal{B}^f$.

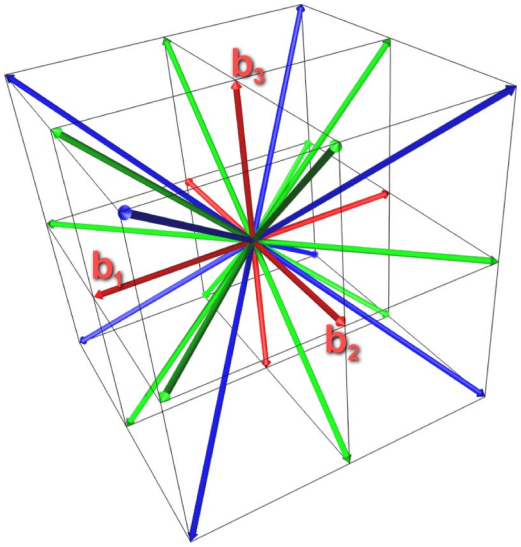

FIG. 1. (Color online) The reciprocal space of a simple cubic lattice. The first (red), second (green), and third (blue) order neighbors are located at the centers of the cube faces, the centers of the cube edges, and the cube corners, respectively. $\vec{b}_1$, $\vec{b}_2$, and $\vec{b}_3$ denote the primitive simple cubic reciprocal lattice vectors.

A. Face-centered cubic structure

We first illustrate the choice of $\mathcal{C}$ coefficients using the fcc Bravais lattice. Since there are only four distinct directions in the $\mathcal{B}^f$ set (blue in Fig. 1), the target vector set can be denoted as $\mathcal{T} = \{\vec{T}_1, \vec{T}_2, \vec{T}_3, \vec{T}_4\}$. One possible choice for the three $\vec{K}_i$ vectors is the following:

$$\vec{K}_1 = \frac{2\pi}{a}(1,1,1),$$

$$\vec{K}_2 = \frac{2\pi}{a}(0,2,0),$$

$$\vec{K}_3 = \frac{2\pi}{a}(-1,1,1). \tag{7}$$

This leads to the choice $\mathcal{T} = \{\vec{K}_1, \vec{K}_3, \vec{K}_{12}, \vec{K}_{23}\}$ and $\mathcal{C} = \{*, 0, *, *, 0, *\}$, where * indicates a nonzero real coeffi-

cient. We denote the nonzero target coefficients as $\mathcal{C}_{\mathcal{T}}=\{\tau_1,\tau_2,\tau_3,\tau_4\}$ so that Eq. (3) becomes

$$\Delta I(\vec{r})=\sum_{i=1}^{4}\tau_i\cos(\vec{T}_i\cdot\vec{r}). \tag{8}$$

Noting that the photonic band structure is invariant to the space group of the crystal, we choose $\mathcal{C}_{\mathcal{T}}$ and find a translation vector, $\vec{\delta}$, such that $\Delta I(\vec{r})$ is invariant under changes of the form $\vec{r}\rightarrow\mathcal{S}^{\mathrm{d}}_{\mathrm{j},\vec{\delta}}(\vec{r})\equiv\mathcal{O}^{\mathrm{d}}_{\mathrm{j}}(\vec{r})+\vec{\delta}$, where we have defined $\mathcal{O}^{\mathrm{d}}=\{\mathcal{O}^{\mathrm{d}}_{\mathrm{j}}\}_{j=\overline{1,48}}$ as the set of fcc point group operations. Such an intensity pattern satisfies the requirement for the smallest possible IBZ. Operating on $\Delta I(\vec{r})$ with $\mathcal{S}^{\mathrm{d}}_{\mathrm{j},\vec{\delta}}$ yields

$$\Delta I(\vec{r})\overset{\mathcal{S}^{\mathrm{d}}_{\mathrm{j},\vec{\delta}}}{\rightarrow}\sum_{i=1}^{4}\tau_i\cos[\vec{T}_i\cdot\mathcal{S}^{\mathrm{d}}_{\mathrm{j},\vec{\delta}}(\vec{r})]=\sum_{i=1}^{4}\tau_i\cos[\mathcal{O}^{\mathrm{r}}_{\mathrm{j}}(\vec{T}_i)\cdot\vec{r}+\xi_i], \tag{9}$$

where $\mathcal{O}^{\mathrm{r}}=\{\mathcal{O}^{\mathrm{r}}_{\mathrm{j}}\}_{j=\overline{1,48}}$ is the set of point group operations of the fcc reciprocal space, and $\{\xi_i=\vec{T}_i\cdot\vec{\delta}\}_{i=\overline{1,4}}$ is a set of four phase factors. Since the target vector set $\mathcal{T}$ is a subset of $\mathcal{K}$, in general the ξ_i are not independent, and are a subset of $\{\gamma_1,\gamma_2,\gamma_3,\gamma_1-\gamma_2,\gamma_1-\gamma_3,\gamma_2-\gamma_3\}$, where $\gamma_i=\vec{K}_i\cdot\vec{\delta}$. In order to simplify the problem, we consider only the case for which $\xi_i\in\{0,\pi\}$, which is consistent with the condition $\xi_i\in\{\gamma_1,\gamma_2,\gamma_3,\gamma_1-\gamma_2,\gamma_1-\gamma_3,\gamma_2-\gamma_3\}$ if one assumes $\gamma_i\in\{0,\pi\}$. For our particular choice of target vectors, it can be verified that $\mathcal{O}^{\mathrm{r}}_{\mathrm{j}}(\vec{T}_i)\in\{\pm\vec{T}_1,\pm\vec{T}_2,\pm\vec{T}_3,\pm\vec{T}_4\}$. Since the sign of $\vec{T}_i$ leaves $\Delta I(\vec{r})$ unchanged, it follows that, for our restricted values of ξ_i, the point group operations $\mathcal{O}^{\mathrm{d}}_{\mathrm{j}}$ simply permute the coefficients $\{\tau_i\}$ as they appear in Eq. (8), in the form

$$\Delta I(\vec{r})=\sum_{i=1}^{4}\tau_i\cos(\vec{T}_i\cdot\vec{r})\overset{\mathcal{S}^{\mathrm{d}}_{\mathrm{j},\vec{\delta}}}{\rightarrow}\sum_{i=1}^{4}\Sigma_k(i)\tau_{\mathcal{P}_j(i)}\cos(\vec{T}_i\cdot\vec{r}),$$

where $\mathcal{P}_j$ is a permutation of the indices {1,2,3,4} completely determined by $\mathcal{O}^{\mathrm{d}}$ and Σ_k is a sign vector defined as

$$\Sigma_k\equiv\{e^{i\gamma_1},e^{i\gamma_2},e^{i\gamma_3},e^{i\gamma_1}-e^{i\gamma_2},e^{i\gamma_1}-e^{i\gamma_3},e^{i\gamma_2}-e^{i\gamma_3}\},$$

where $k=\overline{1,8}$ corresponds to one of the 2^3 possible choices for the $\{\gamma_1,\gamma_2,\gamma_3\}$ set. Invariance of $\Delta I(\vec{r})$ can therefore be determined by requiring $|\tau_i|=1$ for all i and using $\vec{\delta}$ to compensate for any permutation-induced sign changes. The eight Σ_k vectors are given as columns in the following table:

	Σ_1	Σ_2	Σ_3	Σ_4	Σ_5	Σ_6	Σ_7	Σ_8
γ_1	+	−	+	−	+	−	+	−
γ_2	+	+	−	−	+	+	−	−
γ_3	+	+	+	+	−	−	−	−
$\gamma_1-\gamma_2$	+	−	−	+	+	−	−	+
$\gamma_1-\gamma_3$	+	−	+	−	−	+	−	+
$\gamma_2-\gamma_3$	+	+	−	−	−	−	+	+

(10)

The intensity pattern contains four components of Σ_k for some k, with the condition that three of the corresponding phases are independent, such as in the case $\{\gamma_1,\gamma_2,\gamma_1-\gamma_3\}$. According to (10), we can without loss of generality always choose the first three components from Σ_k to be +1. The fcc intensity pattern can then be written as

$$\Delta I_{\mathrm{fcc}}(\vec{r})=\cos(\vec{b}^{\mathrm{f}}_1\cdot\vec{r})+\cos(\vec{b}^{\mathrm{f}}_2\cdot\vec{r})+\cos(\vec{b}^{\mathrm{f}}_3\cdot\vec{r})+\eta\cos[(\vec{b}^{\mathrm{f}}_1+\vec{b}^{\mathrm{f}}_2+\vec{b}^{\mathrm{f}}_3)\cdot\vec{r}], \tag{11}$$

where $\eta=\pm1$ and $\{\vec{b}^{\mathrm{f}}_{\mathrm{i}}\}$ are the primitive vectors of the fcc reciprocal space. The choice $\eta=+1$ leads to an intensity pattern resembling an fcc lattice of spheroid "atoms", as illustrated in Fig. 2(a). This indicates that a fundamental band gap does not open. (It is possible for a higher-order gap to open between bands 5 and 6, characteristic of disconnected $F\bar{4}3m$ structures [64], which are fcc lattices of slightly nonspherical atoms.) On the other hand, the choice $\eta=-1$ produces an intensity pattern, shown in Fig. 2(b), exhibiting a strong resemblance to a diamond network structure and corresponding to the double diamond (D) surface [60]. This is the diamond-like structure studied in previous theoretical reports [56,58,59]. Accordingly, our calculations, presented in the next section, show that a PBG as large as 25% opens between the second and third bands in a structure whose solid component has a dielectric constant of 11.9 (Si). It is

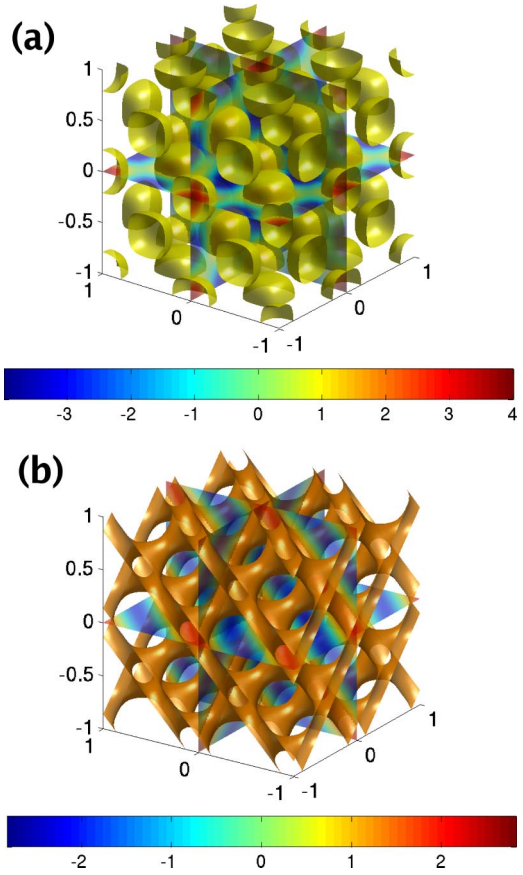

FIG. 2. The iso-intensity surfaces of the fcc structure generated by Eq. (11). (a) An opal-like architecture appears for $\eta=+1$. (b) A diamond-like architecture appears for $\eta=-1$. In both cases, the light intensity is mapped to the color bar.

interesting to note that a single sign in the intensity pattern differentiates between the fcc lattice of spheroids and the diamond structure and therefore determines the existence of a fundamental photonic band gap. In fact, if one extends to noninversion symmetric structures (Sec. III A 2), taking $\eta = 1$ and adding a $\pi/2$ phase to the corresponding cosine term, a structure which retains both a fundamental gap and a gap between bands 5 and 6 can be achieved (see Fig. 5). In the optical interference lithography technique, this sign can be controlled directly though the choice of laser beam amplitude and polarization pairs.

1. Diamond structure

Now that we have obtained the desired intensity pattern, Eq. (11) with $\eta = -1$, it is straightforward to determine holographic beam parameters which produce this pattern. First, it is necessary to determine the wave vectors $\vec{G}_i$ of the incident laser beams, according to Eqs. (1) and (7). The following vectors of length $\sqrt{5}\pi/\underline{a}$ satisfy our requirements:

$$\vec{G}_0 = \frac{\pi}{\underline{a}}(0,-2,-1),$$

$$\vec{G}_1 = \frac{\pi}{\underline{a}}(2,0,1),$$

$$\vec{G}_2 = \frac{\pi}{\underline{a}}(0,2,-1),$$

$$\vec{G}_3 = \frac{\pi}{\underline{a}}(-2,0,1). \tag{12}$$

It is then necessary to determine the polarization vectors which satisfy

$$\{c_1, c_2, c_3, c_{12}, c_{13}, c_{23}\} = \{1,0,1,1,0,-1\} \tag{13}$$

and

$$\{\phi_1, \phi_2, \phi_3, \phi_{12}, \phi_{13}, \phi_{23}\} = \{0,0,0,0,0,0\} \tag{14}$$

[see Eqs. (3) and (4)]. In order to describe the polarization vector for a given $\vec{G}_i$, it is convenient to introduce two mutually perpendicular unit vectors "up", $\vec{U}_i$, and "right", $\vec{R}_i$, to complete an orthogonal triad $(\vec{U}_i, \vec{R}_i, \vec{G}_i,)$ such that

$$\vec{R}_i = \vec{G}_i \times \hat{\mathbf{z}}/|\vec{G}_i \times \hat{\mathbf{z}}|,$$

$$\vec{U}_i = \vec{R}_i \times \vec{G}_i/|\vec{G}_i|,$$

$$\vec{U}_i \times \vec{R}_i = \vec{G}_i/|\vec{G}_i|, \tag{15}$$

where $(\hat{\mathbf{x}}, \hat{\mathbf{y}}, \hat{\mathbf{z}})$ define unit vectors in a specific laboratory coordinate frame. (If $\vec{G}_i \| \hat{\mathbf{z}}$, then by convention we choose $\vec{R}_i = \hat{\mathbf{x}}$.) An elliptical polarization vector can then be expressed as the sum of two linear polarization vectors in the up and right directions:

$$\vec{\epsilon}_i = \cos(\varphi_i)\vec{U}_i + e^{i\beta_i}\sin(\varphi_i)\vec{R}_i, \tag{16}$$

with φ_i describing the relative amplitudes and β_i the relative phase between the two linear polarization vectors. For linear polarizations, the relative phase is zero and hence a linear polarization vector can be expressed as

$$\vec{\epsilon}_i = \cos(\varphi_i)\vec{U}_i + \sin(\varphi_i)\vec{R}_i, \tag{17}$$

where in this case φ_i can be interpreted as a polarization angle.

Beam polarizations and intensities which produce the desired pattern are derived by finding parameters that minimize the intensity background I_0, while satisfying the desired values for the c and ϕ coefficients. If one applies an overall scale to the c coefficients, then the minimal value of I_0, as well as the four beam intensities, will be scaled accordingly. The minimization is performed using a differential evolution method (see, e.g., [65]), which finds a global minimum for I_0. In this method, one generates a randomly distributed set of N-dimensional vectors in the N-dimensional parameter space (in which the constraints on c and ϕ are satisfied). Each vector is "mated" with a random combination of the other vectors to create a trial vector. If the trial vector improves the value of I_0, then it replaces the original vector. The mating step is iterated until the minimum is found. By minimizing I_0 while setting $\{c_1, c_2, c_3, c_{12}, c_{13}, c_{23}\} = \{1,0,1,1,0,-1\}$ and $\{\cos(\phi_1), \cos(\phi_2), \cos(\phi_3), \cos(\phi_{12}), \cos(\phi_{13}), \cos(\phi_{23})\} = \{1,1,1,1,1,1\}$, one arrives at the following elliptical polarization parameters:

$$\{\boldsymbol{\mathcal{E}}_0, \boldsymbol{\mathcal{E}}_1, \boldsymbol{\mathcal{E}}_2, \boldsymbol{\mathcal{E}}_3\} = \{1.29, 1.52, 1.34, 1.08\},$$

$$\{\varphi_0, \varphi_1, \varphi_2, \varphi_3\} = \{34.8°, 66.6°, 40.8°, 14.6°\},$$

$$\{\beta_0, \beta_1, \beta_2, \beta_3\} = \{90.0°, -90.0°, 90.0°, -90.0°\}. \tag{18}$$

These polarizations achieve a value of 6.93 for the intensity background I_0, and the total intensity reaches a maximum of 12.6. It should be noted that this particular numerical solution is not unique [56,58,59]. The beam configuration represented by this solution is shown in Fig. 3. The plane spanned by $\vec{G}_0$ and $\vec{G}_2$ ($\vec{G}_0$-$\vec{G}_2$) is perpendicular to the plane spanned by $\vec{G}_1$ and $\vec{G}_3$ ($\vec{G}_1$-$\vec{G}_3$). The angle between $\vec{G}_0$ and $\vec{G}_2$ equals the angle between $\vec{G}_1$ and $\vec{G}_3$ and has the value 126.9°. The polarization ellipses are shown next to the corresponding beams, depicting the path traced by the polarization vector as one looks down the wave vector. The dashed lines passing through the polarization ellipses lie in the respective planes defined above.

The linear polarization parameters

$$\{\boldsymbol{\mathcal{E}}_0, \boldsymbol{\mathcal{E}}_1, \boldsymbol{\mathcal{E}}_2, \boldsymbol{\mathcal{E}}_3\} = \{2.08, 0.93, 1.29, 2.26\},$$

$$\{\varphi_0, \varphi_1, \varphi_2, \varphi_3\} = \{-29.3°, 6.5°, -46.9°, -100.7°\} \tag{19}$$

also satisfy Eqs. (13) and (14) while minimizing I_0. However, as noted in [59], the ratio I_{max}/I_0 in this case is 17.6/11.97, which is smaller than the one obtained above

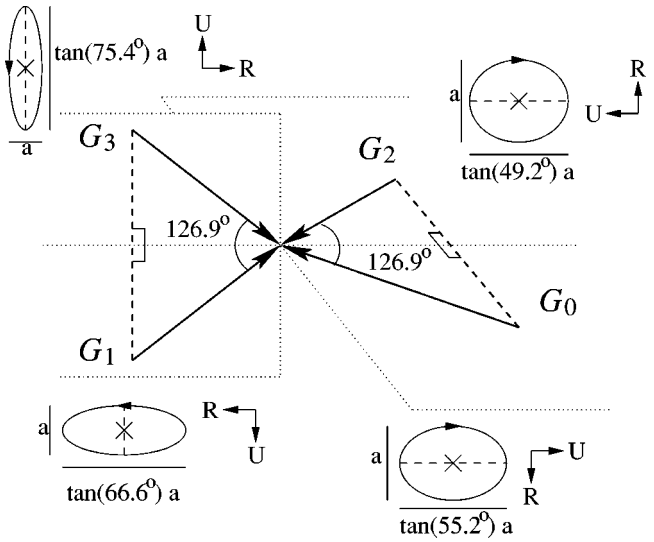

FIG. 3. The diagram of a beam configuration which generates the fcc (diamond) intensity pattern using *elliptically polarized* beams. The plane spanned by $\vec{G}_0$ and $\vec{G}_2$ is perpendicular to the plane spanned by $\vec{G}_1$ and $\vec{G}_3$. The ellipses at the end of each wave vector describe the polarization ellipse of the corresponding beam, as one looks down $\vec{G}_i$, with the dashed line (passing through the polarization ellipse) corresponding to the $\vec{G}_0$-$\vec{G}_2$ or $\vec{G}_1$-$\vec{G}_3$ plane. The $\vec{R}$ and $\vec{U}$ pairs for each beam, defined in Eq. (15), are shown next to the corresponding polarization ellipse.

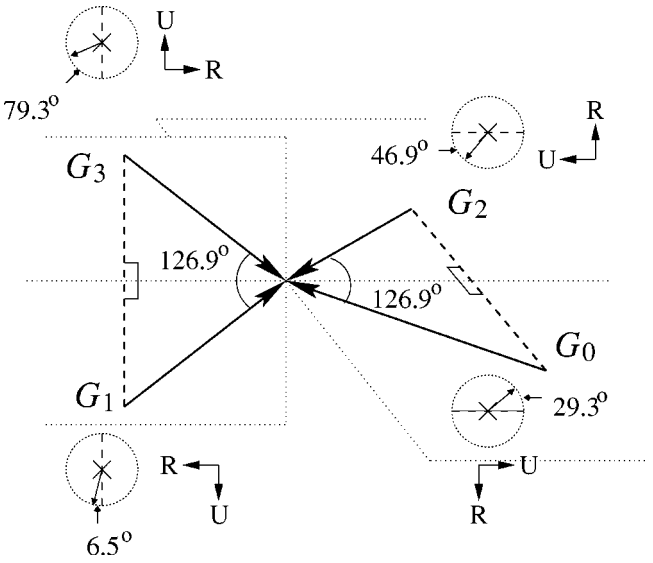

FIG. 4. The diagram of a beam configuration which generates the fcc (diamond) intensity pattern using *linearly polarized* beams. The plane spanned by $\vec{G}_0$ and $\vec{G}_2$ is perpendicular to the plane spanned by $\vec{G}_1$ and $\vec{G}_3$. The polarization angles as one looks down the wave vector are shown next to the corresponding beams, with the dashed line passing through the polarization circle corresponding to the $\vec{G}_0$-$\vec{G}_2$ or $\vec{G}_1$-$\vec{G}_3$ plane. The $\vec{R}$ and $\vec{U}$ pairs for each beam, defined in Eq. (15), are shown next to the corresponding polarization angle.

with elliptical polarizations. This linear polarization beam configuration is shown in Fig. 4. The polarization angles are shown as one looks down the wave vector, relative to the $\vec{G}_0$-$\vec{G}_2$ or $\vec{G}_1$-$\vec{G}_3$ plane.

2. Noninversion symmetric structure

By extending to noninversion symmetric structures it is possible to achieve a connected $F\bar{4}3m$ (corresponding to the space group) structure. This structure has a two-atom basis where, unlike the diamond lattice, the two atoms are disproportionate in size. It has been shown that connected $F\bar{4}3m$ structures display PBGs both between the second and third bands, and between the fifth and sixth bands [64]. The corresponding intensity pattern can be written as

$$\Delta I(\vec{r}) = \cos(\vec{b}_1^{\,f} \cdot \vec{r}) + \cos(\vec{b}_2^{\,f} \cdot \vec{r}) + \cos(\vec{b}_3^{\,f} \cdot \vec{r}) + \cos[(\vec{b}_1^{\,f} + \vec{b}_2^{\,f} + \vec{b}_3^{\,f}) \cdot \vec{r} + \zeta], \tag{20}$$

with $\zeta = \pi/2$. Note that the fcc lattice of spheres and the diamond structure are achieved with $\zeta = 0$ and $\zeta = \pi$, respectively. Figure 5 shows the iso-surface of this intensity pattern which generates a structure with a solid volume fraction of ≈23%, where high intensity regions correspond to the solid parts of the structure. When silicon is used to synthesize the structure in an air background, a 12.5% PBG emerges between bands 2 and 3 (characteristic of the diamond structure achieved with $\zeta = \pi$), and a nearly 5% PBG emerges between bands 5 and 6 (characteristic of the FCC lattice of spheroids achieved with $\zeta = 0$ [64]). The photonic band structure obtained in this case is shown in Fig. 6.

The desired intensity pattern can be obtained by adjusting the polarization vectors and amplitudes of the laser beams used to generate the diamond structure above, while retaining the wave vectors $\vec{G}_i$. In this case, the laser beam amplitude and polarization pairs must obey

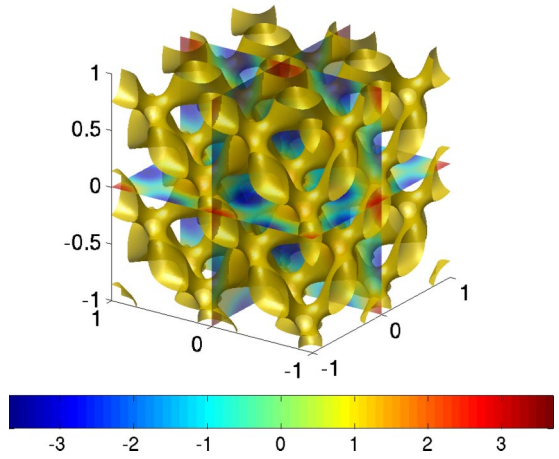

FIG. 5. The iso-intensity surface generated by Eq. (20), with $\zeta = \pi/2$ at a solid volume fraction of ≈23%, with the field intensity mapped to the color bar. When the high intensity regions map to silicon and the low intensity regions to air, this structure displays a 12.5% PBG between bands 2 and 3, and a nearly 5% PBG between bands 5 and 6.

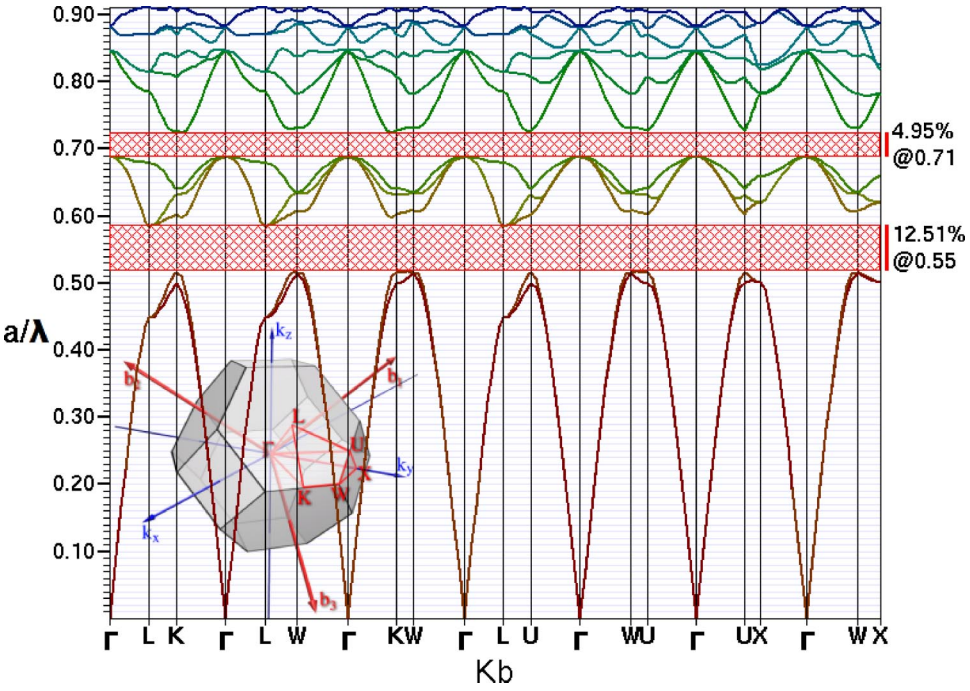

FIG. 6. The photonic band structure diagram for the noninversion symmetric fcc structure shown in Fig. 5 with an 11.9:1 dielectric contrast. The positions of the high symmetry points are shown in the inset.

$$\{c_1, c_2, c_3, c_{12}, c_{13}, c_{23}\} = \{1, 0, 1, 1, 0, 1\} \tag{21}$$

and

$$\{\phi_1, \phi_2, \phi_3, \phi_{12}, \phi_{13}, \phi_{23}\} = \{0, 0, 0, 0, 0, \pi/2\}. \tag{22}$$

Since the structure lacks inversion symmetry, elliptical polarizations must be used. One set of elliptical polarization parameters which minimize I_0 with the constraints imposed by Eqs. (21) and (22) is

$$\{\boldsymbol{\mathcal{E}}_0, \boldsymbol{\mathcal{E}}_1, \boldsymbol{\mathcal{E}}_2, \boldsymbol{\mathcal{E}}_3\} = \{1.36, 1.36, 1.36, 1.36\},$$

$$\{\varphi_0, \varphi_1, \varphi_2, \varphi_3\} = \{37.7°, 37.7°, 37.8°, 37.8°\},$$

$$\{\beta_0, \beta_1, \beta_2, \beta_3\} = \{28.6°, 208.6°, 28.6°208.6°\}. \tag{23}$$

These parameters achieve a value of 7.39 for the intensity background I_0 and a maximum total intensity of 14.78.

Figure 7 shows this beam configuration. The dashed lines passing through the polarization ellipses lie in either the $\vec{G}_0$-$\vec{G}_2$ or $\vec{G}_1$-$\vec{G}_3$ plane. All four ellipses are tilted by an angle of approximately 53.2° from the corresponding plane. In all cases, the major axis is 4.1 times the length of the minor axis.

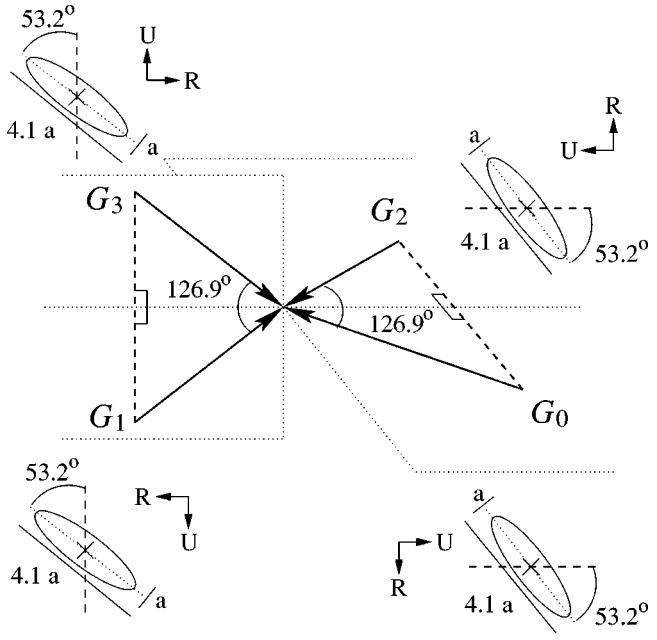

FIG. 7. The diagram of a beam configuration which generates the noninversion symmetric fcc structure. The plane spanned by $\vec{G}_0$ and $\vec{G}_2$ is perpendicular to the plane spanned by $\vec{G}_1$ and $\vec{G}_3$. The ellipses at the end of each wave vector describe the polarization ellipse of the corresponding beam, as one looks down $\vec{G}_i$, with the dashed line (passing through the polarization ellipse) corresponding to the $\vec{G}_0$-$\vec{G}_2$ or $\vec{G}_1$-$\vec{G}_3$ plane. In each case, the major axis of the polarization ellipse (represented by the dotted line passing through the polarization ellipse) is tilted by approximately 53.2° with respect to the corresponding plane. The $\vec{R}$ and $\vec{U}$ pairs for each beam, defined in Eq. (15), are shown next to the corresponding polarization ellipse.

B. Body-centered cubic structure

Next, we consider a holographic structure based on the bcc Bravais lattice. There are six distinct directions in the Green set of vectors in Fig. 1, corresponding to the $\mathcal{B}^b$ set. In order to obtain a nontrivial pattern which possesses the full symmetry of the bcc Bravais lattice, one needs to use all six of these directions. Unfortunately, none of the eight possible combinations for $\mathcal{C}$ generates a structure with a full photonic band gap. It is possible to relax the symmetry conditions by removing the inversion symmetry, which results in the gy-

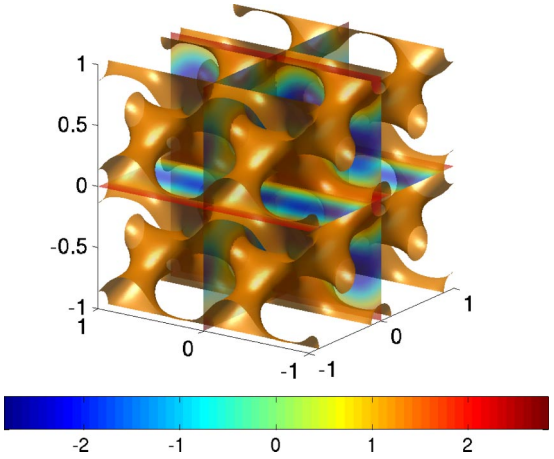

FIG. 8. The optimized bcc architecture generated by Eq. (25) with a solid volume filling fraction of ≈22%. When the solid regions (interior of depicted iso-intensity surfaces) consist of silicon and the background is air, a PBG of 21% is obtained.

roid (G) surface described in [60]. Instead, we relax our symmetry conditions by choosing only four of the six target directions, giving a target vector set $\mathcal{T}=\{\vec{T}_1,\vec{T}_2,\vec{T}_3,\vec{T}_4\}$, which leads to a larger IBZ and an intensity pattern of lower symmetry. One possible choice for the three $\vec{K}_i$ vectors is

$$\vec{K}_1=\frac{2\pi}{\underline{a}}(0,1,1),$$

$$\vec{K}_2=\frac{2\pi}{\underline{a}}(1,1,0),$$

$$\vec{K}_3=\frac{2\pi}{\underline{a}}(1,0,1). \tag{24}$$

This leads to the choice $\mathcal{T}=\{\vec{K}_1,\vec{K}_3,\vec{K}_{12},\vec{K}_{23}\}$, and $\mathcal{C}=\{*,0,*,*,0,*\}$. Using a similar derivation to the one presented in the fcc case but replacing the fcc point group operations with those of the bcc point group, one can write the bcc intensity pattern in terms of the vectors in $\mathcal{T}$ as

$$\Delta I_{\mathrm{bcc}}(\vec{r})=\cos(\vec{T}_1\cdot\vec{r})+\cos(\vec{T}_2\cdot\vec{r})+\cos(\vec{T}_3\cdot\vec{r})+\eta\cos(\vec{T}_4\cdot\vec{r}), \tag{25}$$

where $\eta=\pm1$. The choice $\eta=+1$ produces an intensity pattern resembling a bcc lattice of spheres, which produces no fundamental gap. However, the choice $\eta=-1$ generates a bcc structure whose basis is similar to that of the diamond structure. Figure 8 shows the optimized structure when $\eta=-1$, which produces a PBG of 21% for a silicon structure in an air background.

Holographic beam parameters which produce this intensity pattern are determined straightforwardly as before. The target vectors in $\mathcal{T}$ can be generated by the following $\vec{G}$ vectors of length $\sqrt{3}\pi/\underline{a}$:

$$\vec{G}_0=\frac{\pi}{\underline{a}}(-1,-1,-1),$$

$$\vec{G}_1=\frac{\pi}{\underline{a}}(-1,1,1),$$

$$\vec{G}_2=\frac{\pi}{\underline{a}}(1,1,-1),$$

$$\vec{G}_3=\frac{\pi}{\underline{a}}(1,-1,1). \tag{26}$$

The beam amplitudes and polarizations obey $\{c_1,c_2,c_3,c_{12},c_{13},c_{23}\}=\{1,0,1,1,0,-1\}$ and $\{\phi_1,\phi_2,\phi_3,\phi_{12},\phi_{13},\phi_{23}\}=\{0,0,0,0,0,0\}$. Elliptically polarized beam parameters which obey these constraints and minimize I_0 are

$$\{\boldsymbol{\mathcal{E}}_0,\boldsymbol{\mathcal{E}}_1,\boldsymbol{\mathcal{E}}_2,\boldsymbol{\mathcal{E}}_3\}=\{1.19,1.19,1.19,1.19\},$$

$$\{\varphi_0,\varphi_1,\varphi_2,\varphi_3\}=\{30.0°,30.0°,30.0°,30.0°\},$$

$$\{\beta_0,\beta_1,\beta_2,\beta_3\}=\{90.0°,-90.0°,90.0°,-90.0°\}. \tag{27}$$

It is interesting to note that, with this configuration, the bcc intensity pattern can be created using four laser beams of equal intensities. With this configuration, the intensity background I_0 is 5.66, with the total intensity ranging from 0 to $2I_0$. The beam configuration represented by this solution is shown in Fig. 9. The plane spanned by $\vec{G}_0$ and $\vec{G}_2$ ($\vec{G}_0$-$\vec{G}_2$) is perpendicular to the plane spanned by $\vec{G}_1$ and $\vec{G}_3$ ($\vec{G}_1$-$\vec{G}_3$). The angle between $\vec{G}_0$ and $\vec{G}_2$ equals the angle between $\vec{G}_1$ and $\vec{G}_3$ and has the value 109.5°. The polarization ellipses are shown next to the corresponding beams, depicting the path traced by the polarization vector as one looks down the wave vector. The dashed lines passing through the polarization ellipses lie in the respective planes defined above.

Linearly polarized beams can be used to generate the bcc structure, but, as in the case of the diamond structure, the minimum value of I_0 is larger than in the case of elliptical polarizations. Here, the value of I_0 achieved is 10.17 and the maximum total intensity is 15.83:

$$\{\boldsymbol{\mathcal{E}}_0,\boldsymbol{\mathcal{E}}_1,\boldsymbol{\mathcal{E}}_2,\boldsymbol{\mathcal{E}}_3\}=\{1.11,1.98,1.97,1.09\},$$

$$\{\varphi_0,\varphi_1,\varphi_2,\varphi_3\}=\{-6.1°,21.9°,107.7°,39.7°\}. \tag{28}$$

This linear polarization beam configuration is shown in Fig. 10. Again, the polarization angles are shown as one looks down the wave vector, relative to the $\vec{G}_0$-$\vec{G}_2$ or $\vec{G}_1$-$\vec{G}_3$ plane.

C. Simple cubic

Finally, we consider a holographic structure based on the sc Bravais lattice, which is the simplest of the cubic structures. There are only three distinct directions in the set $\mathcal{B}^s$

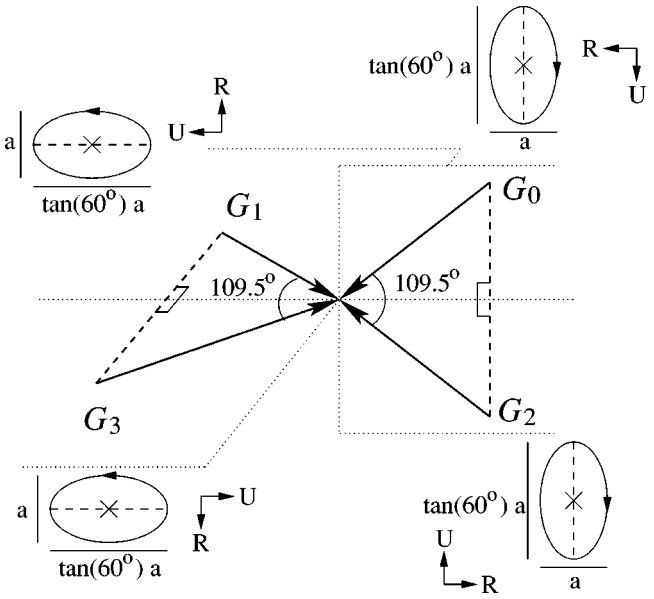

FIG. 9. The diagram of a beam configuration which generates the bcc intensity pattern using *elliptically polarized* beams. The plane spanned by $\vec{G}_0$ and $\vec{G}_2$ is perpendicular to the plane spanned by $\vec{G}_1$ and $\vec{G}_3$. The ellipses at the end of each wave vector describe the polarization ellipse of the corresponding beam, as one looks down $\vec{G}_i$, with the dashed line passing through the polarization ellipse corresponding to the $\vec{G}_0$-$\vec{G}_2$ or $\vec{G}_1$-$\vec{G}_3$ plane. The $\vec{R}$ and $\vec{U}$ pairs for each beam, defined in Eq. (15), are shown next to the corresponding polarization ellipse.

(red set online) of vectors in Fig. 1 and consequently only three vectors in the target vector set, i.e., $\mathcal{T}=\{\vec{T}_1,\vec{T}_2,\vec{T}_3\}$. In this case, we make the simple choice $\vec{T}_i=\vec{K}_i=\vec{b}_i^s$, so that the $\mathcal{C}$

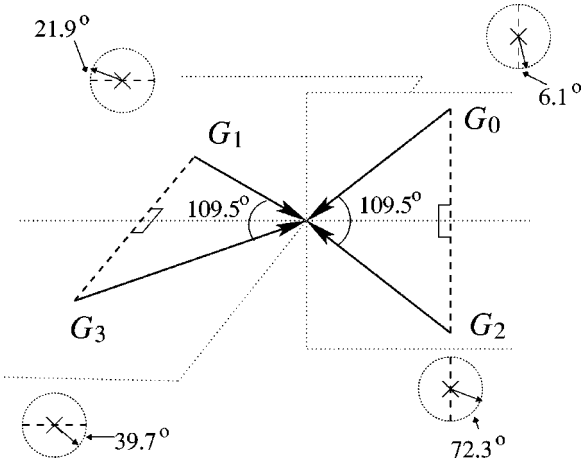

FIG. 10. The diagram of a beam configuration which generates the bcc intensity pattern using *linearly polarized* beams. The plane spanned by $\vec{G}_0$ and $\vec{G}_2$ is perpendicular to the plane spanned by $\vec{G}_1$ and $\vec{G}_3$. The polarization angles as one looks down the wave vector are shown next to the corresponding beams, with the dashed line corresponding to the $\vec{G}_0$-$\vec{G}_2$ or $\vec{G}_1$-$\vec{G}_3$ plane. The $\vec{R}$ and $\vec{U}$ pairs for each beam, defined in Eq. (15), are shown next to the corresponding polarization vector.

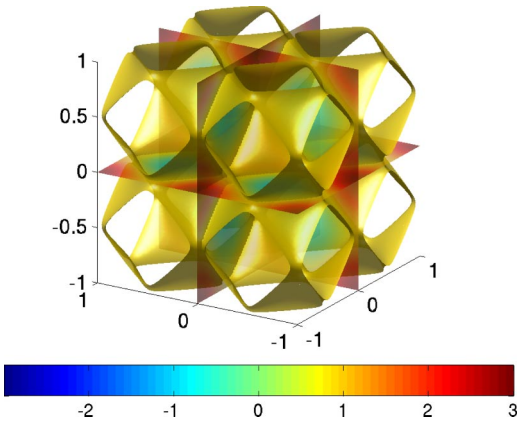

FIG. 11. The optimized sc architecture generated by Eq. (29) with a solid volume filling fraction of ≈24%. When the solid regions (corresponding to regions with a red hue) consist of silicon and the background is air, a PBG of 10.5% is obtained.

coefficients are given by $\mathcal{C}=\{*,*,*,0,0,0\}$, where * denotes a nonzero real coefficient. Again, without loss of generality the first three nonzero coefficients can be chosen to be 1; in this case, this applies to all nonzero coefficients. The intensity pattern is thus given by

$$\Delta I(\vec{r}) = \cos(\vec{T}_1 \cdot \vec{r}) + \cos(\vec{T}_2 \cdot \vec{r}) + \cos(\vec{T}_3 \cdot \vec{r}). \qquad (29)$$

This pattern has a simple cubic Bravais lattice and is invariant to all symmetry operations of the simple cubic point group, thereby satisfying our design requirements. The intensity iso-surface of the optimized Si sc structure is shown in Fig. 11. A full photonic band gap of 10.5% opens between bands 5 and 6 for this optimized structure, which has a solid volume filling fraction of ≈24%.

The target vectors in $\mathcal{T}$ can be generated by the following $\vec{G}$ vectors of length $\sqrt{3}\pi/\underline{a}$:

$$\vec{G}_0 = \frac{\pi}{\underline{a}}(-1,-1,-1),$$

$$\vec{G}_1 = \frac{\pi}{\underline{a}}(1,-1,-1),$$

$$\vec{G}_2 = \frac{\pi}{\underline{a}}(-1,1,-1),$$

$$\vec{G}_3 = \frac{\pi}{\underline{a}}(-1,-1,1), \qquad (30)$$

and beam polarizations which obey $\{c_1,c_2,c_3,c_{12},c_{13},c_{23}\}=\{1,1,1,0,0,0\}$ and $\{\phi_1,\phi_2,\phi_3,\phi_{12},\phi_{13},\phi_{23}\}=\{0,0,0,0,0,0\}$ and minimize I_0 are

$$\{\boldsymbol{\mathcal{E}}_0,\boldsymbol{\mathcal{E}}_1,\boldsymbol{\mathcal{E}}_2,\boldsymbol{\mathcal{E}}_3\}=\{1.79,1.02,1.02,0.88\}$$

$$\{\varphi_0,\varphi_1,\varphi_2,\varphi_3\}=\{50.1°,-7.8°,-67.8°,52.2°\},$$

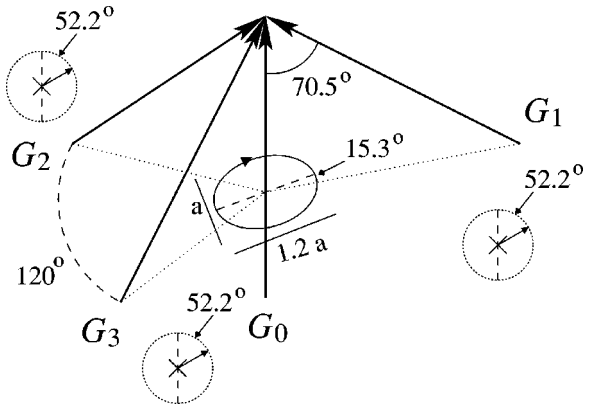

FIG. 12. The diagram of a beam configuration which generates the sc intensity pattern using *elliptically polarized* beams. The beams are set up in an "umbrella" configuration, where $\vec{G}_1$, $\vec{G}_2$, and $\vec{G}_3$ each make an angle of 70.5° with $\vec{G}_0$ and are spread evenly around the azimuth. Beam 0 is elliptically polarized with a polarization ellipse whose major axis is rotated 15.3° from the projection of $\vec{G}_1$ onto the plane normal to $\vec{G}_0$. The other three beams are linearly polarized, with polarization vectors making identical angles of 52.2° with the $\vec{G}_0$-$\vec{G}_i$ planes.

$$\{\beta_0,\beta_1,\beta_2,\beta_3\}=\{275.8°,0°,0°,0°,\}. \tag{31}$$

In this case, an "umbrella" configuration of the beams is used (see Fig. 12). Each of the wave vectors $\vec{G}_1$, $\vec{G}_2$, and $\vec{G}_3$ makes an angle of 70.5° with $\vec{G}_0$ and is spread evenly around the azimuth. Only beam 0 is elliptically polarized; the major axis of the polarization ellipse (depicted as the dashed line passing through the polarization ellipse) makes an angle of 15.33° with the projection of $\vec{G}_1$ onto the plane normal to $\vec{G}_0$. The other three beams are linearly polarized, with polarization vectors making identical angles of 52.24° with the $\vec{G}_0$ -$\vec{G}_i$ planes. The background intensity I_0 is 6.07, and the total intensity ranges from 0.07 to 12.07.

If one constrains all four polarizations to be linear, the parameters

$$\{\mathcal{E}_0,\mathcal{E}_1,\mathcal{E}_2,\mathcal{E}_3\}=\{1.92,0.64,1.28,1.28\},$$

$$\{\varphi_0,\varphi_1,\varphi_2,\varphi_3\}=\{-15.5°,67.8°,7.7°,-52.2°\} \tag{32}$$

yield a minimum value of 7.35 for I_0, with the maximum total intensity reaching 13.35. The linear beam configuration is shown in Fig. 13.

IV. GENERALIZED TETRAGONAL STRUCTURES

The diamond (fcc) and bcc structures described in Sec. III can be considered as special cases of a larger class of photonic crystals. The varying intensity pattern associated with these structures can be written as

$$\Delta I(\vec{r})=\cos(\vec{T}_1\cdot\vec{r})+\cos(\vec{T}_2\cdot\vec{r})+\cos(\vec{T}_3\cdot\vec{r})-\cos(\vec{T}_4\cdot\vec{r}), \tag{33}$$

where the target vectors, $\vec{T}_i$, are given by

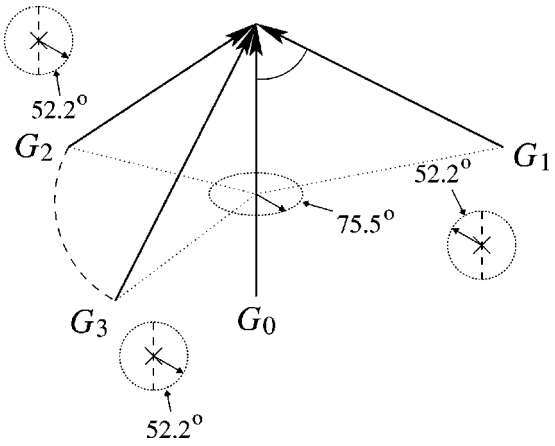

FIG. 13. The diagram of a beam configuration which generates the sc intensity pattern using *linearly polarized* beams. Each of the wave vectors $\vec{G}_1$, $\vec{G}_2$, and $\vec{G}_3$ make an angle of 70.5° with $\vec{G}_0$ and are spread evenly around the azimuth. The polarization angle of beam 0 is measured with respect to the projection of $\vec{G}_1$ onto the plane normal to $\vec{G}_0$, whereas the other polarization angles are measured with respect to the $\vec{G}_i$-$\vec{G}_0$ plane, for i=1,…,3, with the wave vector pointing into the page.

$$\vec{T}_1=\left(-\frac{2\pi}{\underline{a}},\frac{2\pi}{\underline{a}},\frac{2\pi}{\underline{c}}\right),$$

$$\vec{T}_2=\left(\frac{2\pi}{\underline{a}},-\frac{2\pi}{\underline{a}},\frac{2\pi}{\underline{c}}\right),$$

$$\vec{T}_3=\left(\frac{2\pi}{\underline{a}},\frac{2\pi}{\underline{a}},-\frac{2\pi}{\underline{c}}\right),$$

$$\vec{T}_4=\left(\frac{2\pi}{\underline{a}},\frac{2\pi}{\underline{a}},\frac{2\pi}{\underline{c}}\right). \tag{34}$$

The general structure can be modeled in a tetragonal unit cell whose aspect ratio is given by the quantity $\underline{c}/\underline{a}$. By varying the aspect ratio, one can scale the structure along the z direction. The aspect ratio can be written in terms of the acute angle between any one of the target vectors and the z axis, ξ, by

$$\underline{c}/\underline{a}=|\tan(\xi)|/\sqrt{2}. \tag{35}$$

The diamond structure is achieved when $\xi=\arctan(\sqrt{2})=54.7°$ (corresponding to $\underline{c}/\underline{a}=1$) and the bcc structure results when $\xi=45°$ (corresponding to $\underline{c}/\underline{a}=1/\sqrt{2}$).

The desired target vectors can be obtained by changing the angle between wave vectors, which we denote by ν, in the counter-propagating scheme used for the fcc and bcc structures described in Sec. III (see, e.g., Fig. 3). For target vectors characterized by a given ξ, an angle ν given by

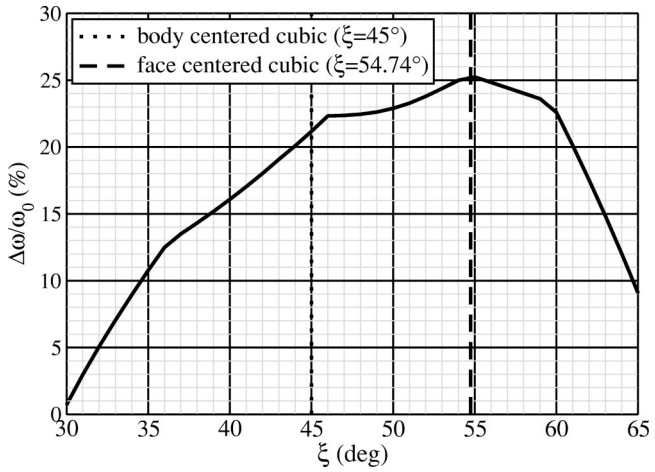

FIG. 14. The relative size of the full photonic band gap as a function of the angle, ξ, between the target vectors, $\vec{T}_i$, and the z axis. The structure has a solid volume fraction of 22.1%. The solid has a dielectric constant of 11.9, corresponding to silicon. The bcc structure corresponds to $\xi=45°$ and the diamond (fcc) structure corresponds to $\xi=54.74°$.

$$\nu = 2\arccos\left(\frac{\cos(\xi)}{\sqrt{2-\cos^2(\xi)}}\right) \tag{36}$$

is sufficient. As shown in Figs. 3 and 9, angles between wave vectors of 126.9° and 109.5° satisfy the conditions for fcc and bcc structures, respectively. Beam polarizations which satisfy the constraints $\{c_1,c_2,c_3,c_{12},c_{13},c_{23}\}=\{1,0,1,1,0,-1\}$ and $\{\cos(\phi_1),\cos(\phi_2),\cos(\phi_3),\cos(\phi_{12}),\cos(\phi_{13}),\cos(\phi_{23})\}=\{1,1,1,1,1,1\}$ can then be found using the minimization procedure described previously.

Figure 14 shows the size of the relative photonic band gap as ξ varies, for structures with a dielectric contrast of 11.9 to 1, corresponding to silicon in air. The solid volume fraction in all cases is 22.1%. The maximum PBG occurs at $\xi=54.74°$, which is the diamond structure. Figure 15 shows the photonic band structure for a structure with $\xi=50°$, between the bcc and fcc cases. A full photonic band gap of 23% opens for this structure.

V. ROBUSTNESS OF HOLOGRAPHIC PHOTONIC CRYSTALS

We now turn our attention to the properties of the inversion symmetric holographic photonic crystals obtained from the intensity patterns derived in the previous section. For a given intensity pattern, it is first necessary to determine the optimal value of the threshold I_{thr} in the simplified shape function, Eq. (5). The choice of I_{thr} corresponds to choosing a particular iso-intensity surface, and therefore the solid volume filling fraction of the resulting crystal. The one-to-one mapping from the I_{thr} to the volume fraction is displayed in Fig. 16 for the fcc, bcc, and sc structures. The functional dependence of the volume fraction (measured in %) on I_{thr} is not strictly linear, but can be taken to be so for the volume fractions of interest. The linear part of the mapping can be written as

$$f^f = -21I_{\text{thr}} + 50,$$

$$f^b = -21I_{\text{thr}} + 50,$$

$$f^s = -29I_{\text{thr}} + 50, \tag{37}$$

where f^f, f^b, and f^s are the volume fractions of the fcc, bcc, and sc structures, respectively. Since the fcc and bcc structures are both specific examples of the generalized structure described in Sec. IV, the mapping is identical for the two

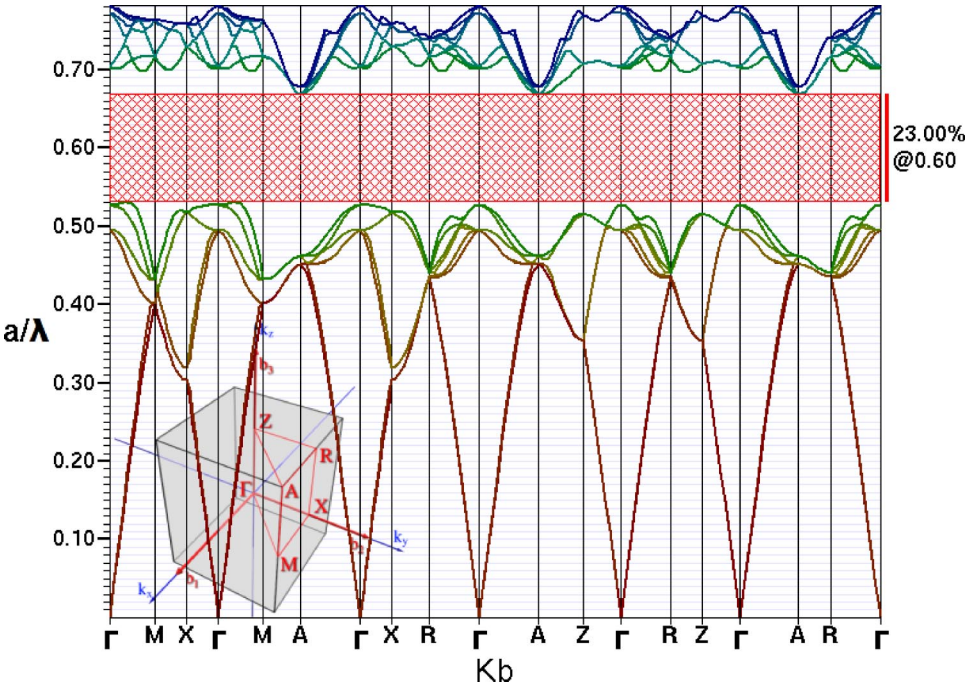

FIG. 15. The photonic band structure of the generalized structure with $\xi=50°$, at a solid volume fraction of 22.1% and a dielectric contrast of 11.9 to 1, corresponding to silicon. The high symmetry points and the irreducible Brillouin zone are shown in the inset. This exhibits a PBG of 23%.

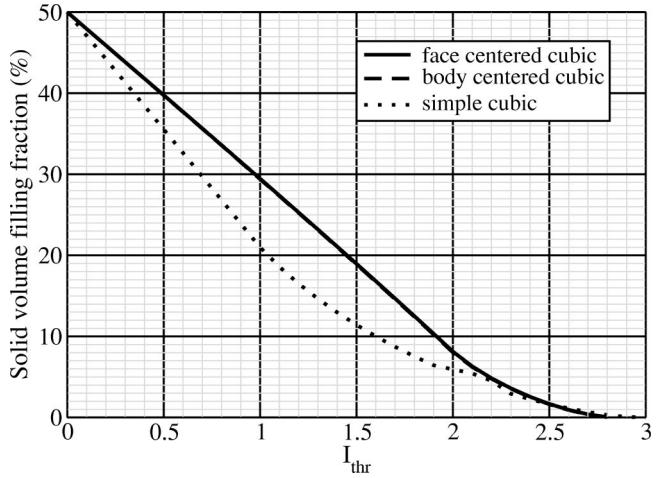

FIG. 16. The volume solid versus threshold used in the shape function Eq. (5), for fcc, bcc, and sc structures. The fcc and bcc curves overlap each other because both structures are members of the generalized HLPC structures described in Sec. IV. The solid material is found in the regions where $\Delta I(\vec{r}) > I_{\text{thr}}$.

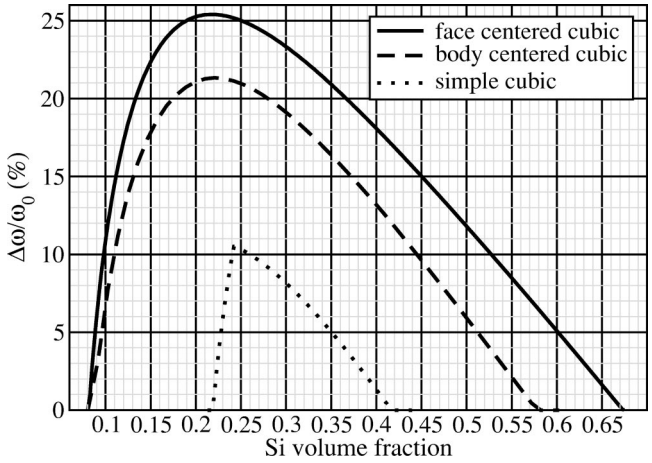

FIG. 17. The relative size of the full photonic band gap as a function of the solid volume fraction, for the fcc, bcc, and sc structures. The solid has a dielectric constant of 11.9, corresponding to silicon. The optimized fcc structure is ≈21.5% solid and generates a relative gap of 25%. The optimized bcc structure is ≈22% solid and generates a relative gap of 21%. The optimized sc structure is ≈24% solid and generates a relative gap of 10.5%.

structures. One may note that this mapping is symmetric around a volume fraction of 50%. In fact, it can be shown that, for the three cubic structures we have obtained, taking $I_{\text{thr}} \rightarrow -I_{\text{thr}}$ produces an equivalent but inverted structure (solid and air regions are interchanged), to within a translation of the origin. In terms of a physical (experimentally measured) intensity, this corresponds to $I_{\text{thr}}^{\text{expt}} \rightarrow 2I_0 - I_{\text{thr}}^{\text{expt}}$. This implies that the desired structure can be achieved equivalently by both single and double inversion processes simply by adjusting the threshold value accordingly. Similarly, this means that one can compensate for the distinction between positive and negative photo-resist materials by changing the holographic exposure time or overall intensity. Consider the shape functions S_d of the direct structure and S_i of the inverted structure, given by

$$S_d(\vec{\mathrm{r}}, I_{\text{thr}}) = \Theta(\Delta I(\vec{\mathrm{r}}) - I_{\text{thr}}),$$

$$S_i(\vec{\mathrm{r}}, I_{\text{thr}}) = \Theta(I_{\text{thr}} - \Delta I(\vec{\mathrm{r}})). \tag{38}$$

We endeavour to find $\vec{\rho} = \vec{\mathrm{r}}' - \vec{\mathrm{r}}$ such that $S_d(\vec{\mathrm{r}}, I_{\text{thr}}) = S_i(\vec{\mathrm{r}}', -I_{\text{thr}})$. This implies that $\Delta I(\vec{\mathrm{r}}') = -\Delta I(\vec{\mathrm{r}})$. This condition is met provided that

$$\vec{K}_{\mathrm{i}} \cdot \vec{\rho} = (2n_i + 1)\pi$$

$$\vec{K}_{\mathrm{ij}} \cdot \vec{\rho} = (2n_{ij} + 1)\pi, \tag{39}$$

where n_i and n_{ij} are integers, for all i such that $c_i \neq 0$ and all i, j such that $c_{ij} \neq 0$. Recall that c_i and c_{ij} are the members of the set $\mathcal{C}$ defined in Eq. (6). Equation (39) can only be satisfied if, when c_{ij} is nonzero, either c_i or c_j is zero. The format of the set $\mathcal{C}$ of the three inversion symmetric structures discussed above satisfies this condition. It can be shown that the corresponding translation vectors, $\vec{\rho}$, are $\vec{\rho}_f = (a/2, a/2, a/2)$ for the fcc structure, $\vec{\rho}_b = (a/2, a/2, 0)$, for the bcc structure, and $\vec{\rho}_s = (a/2, a/2, a//2)$, for the sc structure.

Figure 17 displays the relative size of the full photonic band gap as a function of the solid volume fraction for the fcc, bcc, and sc structures composed of a material with a dielectric constant of 11.9 (Si) in an air background. The optimized fcc structure occurs at a solid volume fraction ≈21.5% and has a relative fundamental gap (between the second and third bands) of 25%. The optimized bcc structure, which is ≈22% solid, also has a fundamental gap, which is 21% of the gap center frequency in this case. Finally, for a solid volume fraction of ≈24%, a full photonic band gap of 10.5% opens between bands 5 and 6 for the optimized sc structure. The photonic band structure diagrams for the three optimized structures are shown in Fig. 18. Figure 19 shows the dependence of the relative photonic band gap on the index of refraction of the solid material for the three optimized structures. For the fcc structure, a full photonic band gap appears when the refractive index is larger than about 1.97. The relative width increases with the index of refraction until saturation at about 38%. The refractive index threshold for the bcc structure is approximately 2.24 and the relative PBG saturates at 34%. The index threshold for the sc structure is 2.77 and the relative PBG saturates at 16.5%.

The global intensity contrast, defined as $\max(|2\Delta I(\vec{\mathrm{r}})|)/I_0$, is of important practical concern. The larger the contrast, the more effective the developing process to create the polymer photonic crystal template. An alternative metric for measuring the global intensity contrast can be found in [58]. The intensity contrast depends both on the shape being created and on the particular beam configuration used to create that shape. Table I shows the global intensity contrast for each of the beam configurations for the inversion symmetric structures discussed in Sec. III. For each structure, the use of elliptically polarized beams improves the contrast over the case when only linearly polarized beams are used. The elliptical beam configuration for the bcc structure achieves a

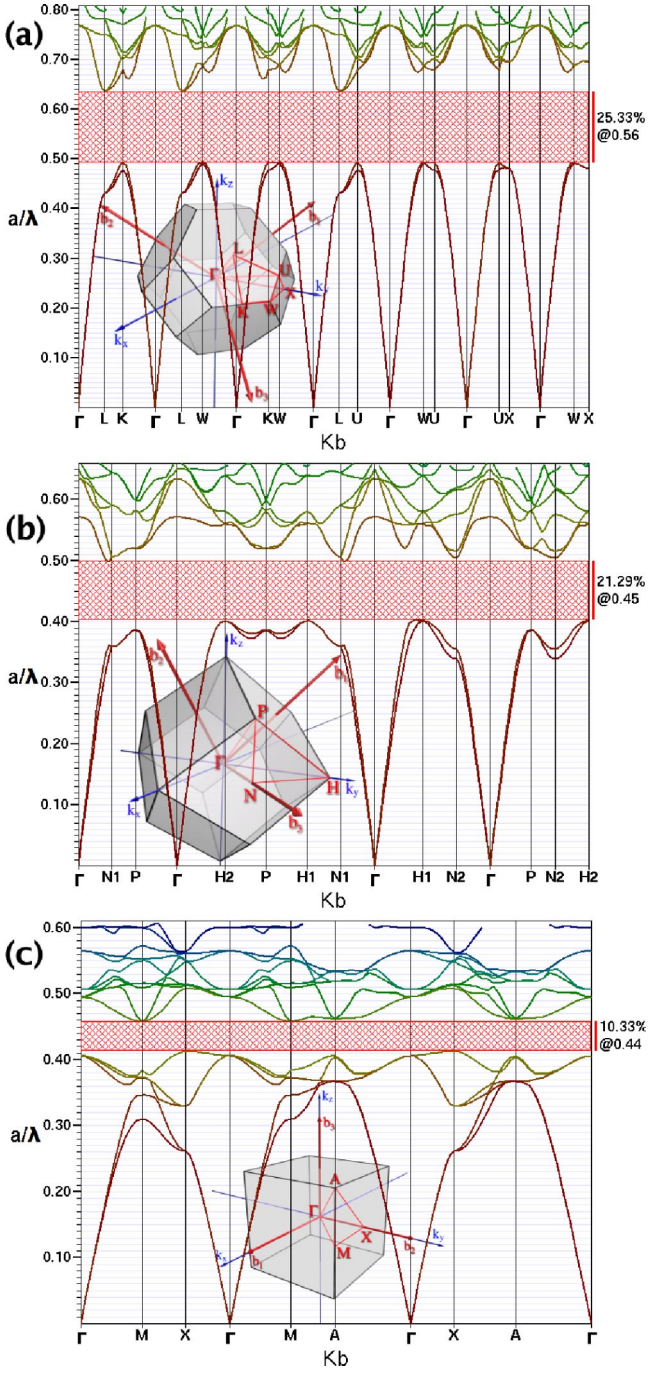

FIG. 18. Photonic band structure diagrams for the optimized (a) fcc, (b) bcc, and (c) sc holographic photonic crystals structures characterized by an 11.9:1 dielectric contrast. The positions of the high symmetry points together with the corresponding irreducible Brillouin zones are shown in the insets.

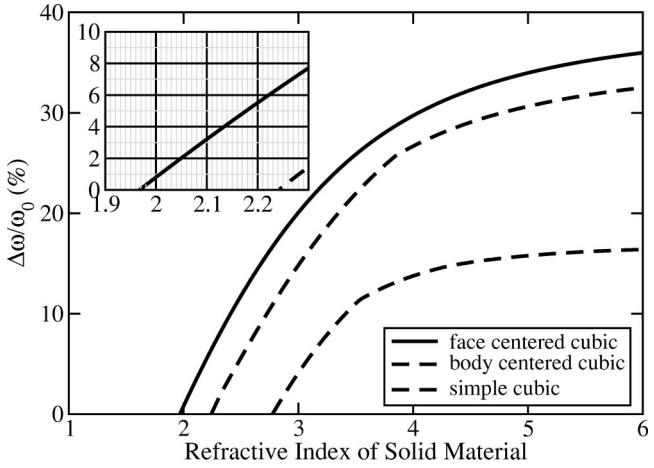

FIG. 19. The relative size of the full photonic band gap as a function of the index of refraction of the solid material, for the optimized fcc, bcc, and sc structures. The background is assumed to be air. The threshold index of refraction for the emergence of a photonic band gap is 1.97 for the fcc structure, 2.24 for the bcc structure, and 2.77 for the sc structure. The inset shows a magnified view of the curve, near the threshold indices of refraction for the fcc and bcc structures.

"perfect" contrast ratio of 1, meaning that a value of zero total intensity is found in the interference pattern.

When comparing the exposure efficiency of different interference patterns, it is not sufficient to consider only the global intensity contrast. Disorder in the PBG template may arise from polymer inhomogeneities that lead to small, random variations in the exposure threshold from point to point in the bulk photo-resist. This, in turn, may cause "roughening" of the interface between "exposed" and "unexposed" polymer even though the iso-intensity contours are perfectly smooth. Therefore, it is useful to maximize the gradient of the intensity pattern at precisely the threshold intensity isosurface. This minimizes the spatial extent of "exposure roughening". In order to compare the intensity contrasts for the fcc, bcc, and sc structures, we define an average intensity contrast factor for an iso-intensity surface at I_{thr}, $C_{avg}(I_{\text{thr}})$ as

$$C_{avg}(I_{\text{thr}}) = \frac{\int_{\partial V} \vec{\nabla}[\Delta I(\vec{r})] \cdot d\vec{A}}{(I_0 + 2I_{\text{thr}}) \int_{\partial V} \vec{n} \cdot d\vec{A}}, \tag{40}$$

where V corresponds to the region which becomes the interior of the resulting structure and ∂V corresponds to its surface (i.e., the iso-intensity surface). In other words, the con-

TABLE I. Global intensity contrast in the interference patterns of the various beam configurations. The global intensity contrast is defined as the ratio of the amplitude of the varying part of the intensity, $\max(|2\Delta I(\vec{r})|)$, and the background intensity I_0. The use of elliptical polarizations improves the global intensity contrast for each of the three structures.

Structure	Polarizations	I_0	$\max(\lvert 2\Delta I(\vec{r})\rvert)$	Contrast
fcc	elliptical	$4\sqrt{3}$	$4\sqrt{2}$	0.816
	linear	11.97	$4\sqrt{2}$	0.472
bcc	elliptical	$4\sqrt{2}$	$4\sqrt{2}$	1
	linear	10.17	$4\sqrt{2}$	0.556
sc	elliptical	6.06	6	0.989
	linear	7.35	6	0.816

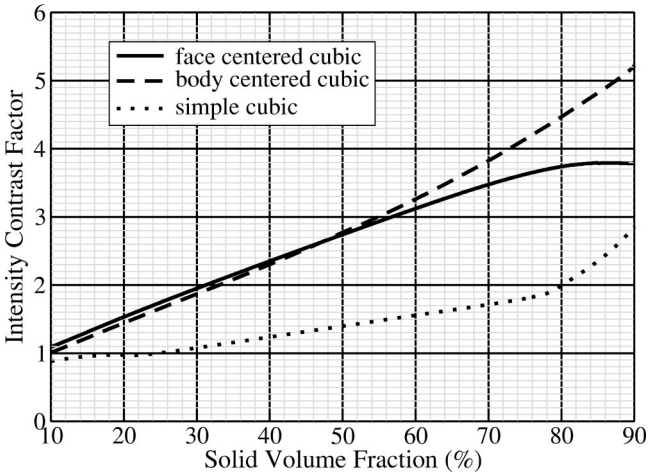

FIG. 20. The plot of the average intensity contrast factor, C_{avg}, as a function of the volume fraction of solid for the fcc, bcc, and sc structures, created using elliptically polarized beams which produce minimal background intensities. The solid part of the photonic crystal corresponds to regions where the intensity exceeds the threshold value.

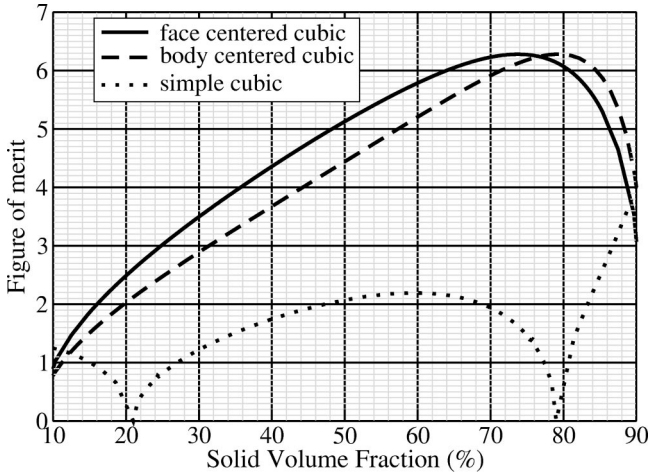

FIG. 21. The plot of the minimum intensity contrast $C_{min} = \min_{\Delta I(\vec{r})=I_{thr}} |\vec{\nabla}[\Delta I(\vec{r})]/(I_0+2I_{thr})|$ as a function of the solid volume fraction for the fcc, bcc, and sc intensity patterns which produce minimal background intensities using elliptically polarized beams.

trast factor gives the average value of the intensity gradient along the iso-intensity surface, normalized by the iso-intensity value. Normalization by the iso-intensity value means that the contrast factor is not symmetric with respect to a solid volume fraction of 50%. Using Gauss' theorem and taking the area of the iso-intensity surface as A, the contrast factor can be rewritten as

$$C_{avg} = \frac{1}{(I_0 + 2I_{\mathrm{thr}})A} \int_V \vec{\nabla}^2[\Delta I(\vec{r})]dV. \tag{41}$$

Figure 20 shows a plot of the average intensity contrast factor, C_{avg}, as a function of the volume fraction of solid for the fcc, bcc, and sc structures. The contrast factor is calculated by discretizing the conventional (cubic) unit cell in 256^3 boxes and sampling the appropriate intensity pattern. The area of the iso-intensity surface in the cubic cell is calculated by approximating the surface with a triangular mesh. The volume integral is calculated by taking

$$\int_V \vec{\nabla}^2[\Delta I(\vec{r})]dV \rightarrow \sum_{\Delta I(\vec{r}) \leqslant I_{\mathrm{thr}}} \vec{\nabla}^2[\Delta I(\vec{r})]v,$$

where v is the volume of the small voxels and $\vec{\nabla}^2[\Delta I(\vec{r})]$ is calculated analytically from the corresponding intensity pattern. The solid part of the photonic crystal corresponds to regions where the intensity exceeds the threshold value. This could be achieved using negative photo-resists and double inversion. Near the respective optimal solid volume fractions ($\approx$22%), the contrast factors for the fcc and bcc structures are approximately equal and larger than the sc contrast factor. However, near 78% solid volume fraction (which corresponds to the inverted structure), the bcc contrast factor becomes larger than the fcc contrast factor. This is relevant if a single inversion process is used in conjunction with a negative photo-resist, or if double inversion is used with a positive photo-resist.

In addition to considering average intensity gradient, we examine the minimum intensity gradient for various iso-intensity surfaces by finding the figure of merit [14]:

$$C_{min} = \min_{\Delta I(\vec{r})=I_{\mathrm{thr}}} |\vec{\nabla}[\Delta I(\vec{r})]/(I_0 + 2I_{\mathrm{thr}})|. \tag{42}$$

This is calculated analytically for every point on the triangular mesh used to approximate a given iso-intensity surface. The regions where contrast is minimum along the threshold iso-intensity surface represent the weak points of the photonic crystal template. These regions are most susceptible to disorder in the holographic process. Shown in Fig. 21, C_{min} gives a measure of the worst case for each iso-intensity surface. In this case, the fcc interference pattern has the best characteristics near the optimized volume fraction of 22%, whereas the fcc and bcc patterns have similar characteristics near 78% volume fraction. It should be noted that the sc interference pattern appears to achieve the worst case near both the optimized direct and inverted volume fractions.

Finally, we consider the sensitivity of the holographic photonic crystals to imprecision in the laser beam parameters. We do this by considering the trajectories of the photonic band edges as beam polarizations and amplitudes are perturbed from the optimal configurations. Figure 22 shows the photonic band edges of the fcc, bcc, and sc structures as a single beam amplitude is perturbed from the optimal value. Only the worst (most sensitive) case out of the four possible beam perturbations is shown for each of the structures. The fcc structure shows the most robustness against amplitude perturbations, allowing the single beam amplitude to range from 70% to 250% of the optimal value before the gap closes, with the bcc structure showing similar characteristics. On the other hand, a 10% perturbation in the single beam amplitude closes the gap in the case of the sc structure. Next, we consider perturbations to the polarization vectors in the

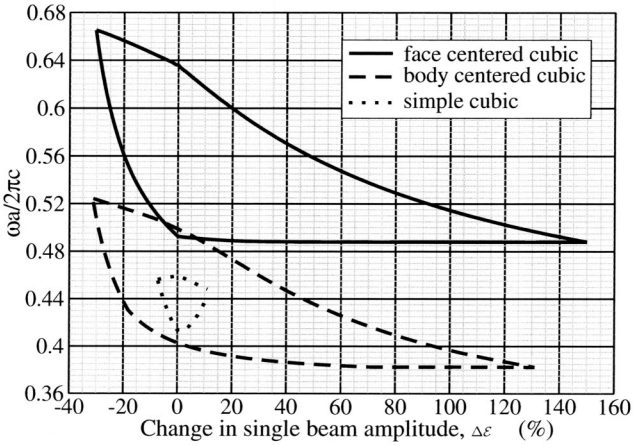

FIG. 22. The photonic band edges of the optimized fcc, bcc, and sc structures as functions of perturbations in the holographic beam amplitudes, $\Delta\mathcal{E}_i$. The structure is assumed to consist of a material of dielectric constant 11.9 in an air background.

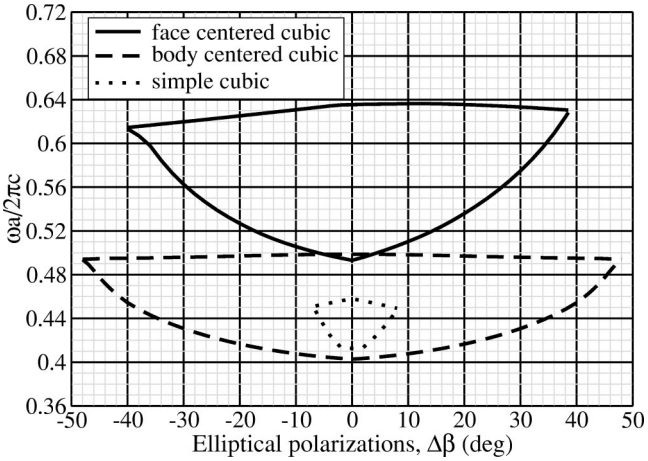

FIG. 24. The photonic band edges of the optimized fcc, bcc, and sc structures as functions of perturbations in the angle β [see Eq. (16)]. The structure is assumed to consist of a material of dielectric constant 11.9 in an air background.

optimal elliptically polarized beam configurations used to create the structures described in this paper. Recall Eq. (16) where we write an elliptical polarization vector as the sum of two linear polarizations such that $\vec{\epsilon}=\cos(\varphi)\vec{U}+e^{i\beta}\sin(\varphi)\vec{R}$. Figure 23 shows the photonic band edges of the three structures when the quantity $\tan(\varphi)$, which describes the relative amplitude of the two linear components, is perturbed from the optimal value. The dependence of the photonic band edges on perturbations of β, the relative phase between the linear polarization components, is shown in Fig. 24. For both graphs, only the worst case out of the four possible perturbations for each structure is displayed. For these elliptically polarized beam configurations, it is noted that the photonic band gap of the bcc structure is most robust against beam parameter perturbations, while the sc structure displays the least robustness. Finally, we consider perturbations to a single polarization angle, φ, for the optimal linearly polarized beam configurations in Fig. 25, by changing the polarization angle of a single beam. Figure 25 shows the photonic band edges of the inversion symmetric fcc, bcc, and sc structures as the polarization angle of the most sensitive beam is perturbed. In the worst case, the photonic band gap of the bcc structure remains open after an 8° change in a single polarization angle, whereas for the fcc structure, a 6° perturbation closes the gap. Again, the sc structure is least robust.

VI. CONCLUSION

In summary, we have derived beam configurations for creating fcc, bcc, and sc photonic crystals using holographic lithography through simple, intuitive symmetry considerations. The guiding principle in this procedure is that a large PBG can be obtained by choosing a structure with the smallest possible irreducible Brillouin zone. The fcc structure, which resembles the diamond network structure, exhibits a

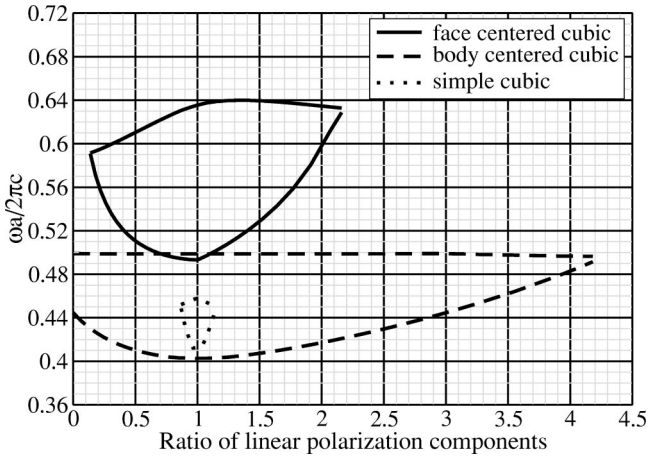

FIG. 23. The photonic band edges of the optimized fcc, bcc, and sc structures as functions of perturbations in the ratio $\tan(\varphi)$ [see Eq. (16)]. The structure is assumed to consist of a material of dielectric constant 11.9 in an air background.

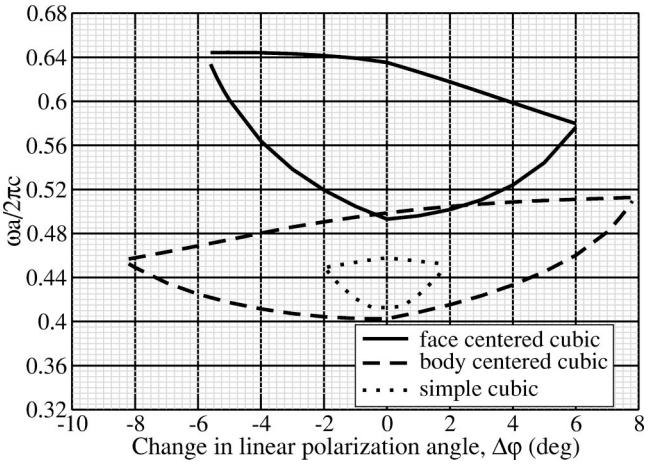

FIG. 25. The photonic band edges of the optimized fcc, bcc, and sc structures as functions of perturbations in single linear polarization angles φ. The structure is assumed to consist of a material of dielectric constant 11.9 in an air background.

full photonic band gap of 25% when made with materials with a dielectric contrast of 11.9:1. Our results also reveal that an optimized geometrical structure within the unit cell enables the bcc lattice to exhibit a PBG comparable to that of the widely studied diamond lattice. Here the photonic band gap is 21% for materials with a dielectric contrast of 11.9:1. Finally, we have found a simple cubic holographic architecture which exhibits a PBG of roughly 11% in the case of Si:air materials. This sc PBG material can be achieved using a simple "umbrella configuration" for the interfering laser beams. In each case, we find that an equivalent but inverted structure can be achieved simply by changing the threshold intensity. This implies that there need be no distinction between direct structures and structures made by inversion techniques. The beam configurations which we describe are optimal with respect to maximizing the intensity contrast in the respective laser interference patterns. The fcc and bcc structures exhibit similar contrast near the optimal filling fractions, while the sc structure displays worse contrast. For all three structures, the use of elliptically polarized beams enables better intensity contrast than can be achieved by the use of linearly polarized beams alone. We have also studied the sensitivity of our holographic structures to perturbations of the amplitudes and polarization angles of the holographic laser beams. The fcc and bcc structures each continue to exhibit full photonic band gaps even as a single linear polarization angle is adjusted by 6° or a single beam amplitude is adjusted between 70% and 240% of the optimal value. These structures also show robustness against perturbations in a single polarization when elliptical polarizations are used. These results suggest that holographic lithography provides a fault-tolerant approach to PBG micro-fabrication.

All three of the structures we describe yield photonic band gaps centered at wavelengths approximately twice the wavelength of the incident interfering laser beams. Therefore, in order to achieve PBGs at the 1.55 μm wavelength preferred for telecommunications, it is necessary to use a photo-resist or other photo-polymerizable material which can be exposed by laser beams of wavelength of about 750 nm. The SU-8 negative photo-resist which has been used in several experimental studies [13,47,49] is intended for near-ultraviolet rather than near-infrared lithography [66]. Other issues to be considered are the postprocessing (infiltration and inversion) limitations imposed on the final, high-index structure. For example, in some architectures, an infiltration process may not be able to produce complete inversions of a template, and pockets of air may persist in thicker regions of the infiltrating material (partial inversion). The presence of such imperfections may have a deleterious effect on the optical properties of the resulting photonic crystal.

Finally, it is of considerable interest to incorporate line and point defects into photonic crystals for use in optical microchips. Photonic crystal templates created using optical interference lithography offer a unique opportunity for the inclusion of such defects. After the photo-resist has been exposed by interference patterns such as those described in this paper, a localized exposure technique such as direct laser writing [34,35] by two-photon absorption can be used to pattern the photo-resist further with the desired defects. In such a scheme, defects can be introduced at the templating stage into the bulk photo-resist, rather than after the photonic crystal has been synthesized. In the latter situation, complications can arise due to scattering of the "writing" laser beam at the numerous air-dielectric interfaces. These possibilities suggest that optical interference lithography together with direct laser writing can provide a powerful platform for the eventual creation of optical microchips containing circuits of light in a photonic band gap.

ACKNOWLEDGMENT

This work was supported in part by the National Sciences and Engineering Research Council of Canada.

[1] Sajeev John, Phys. Rev. Lett. **58**, 2486 (1987).
[2] Eli Yablonovitch, Phys. Rev. Lett. **58**, 2059 (1987).
[3] Sajeev John, Phys. Rev. Lett. **53**, 2169 (1984).
[4] S. John and J. Wang, Phys. Rev. Lett. **64**, 2418 (1990).
[5] Alongkarn Chutinan, Sajeev John, and Ovidiu Toader, Phys. Rev. Lett. **90**, 123901 (2003).
[6] Attila Mekis, J. C. Chen, I. Kurland, Shanhui Fan, Pierre R. Villeneuve, and J. D. Joannopoulos, Phys. Rev. Lett. **77**, 3787 (1996).
[7] M. M. Sigalas, R. Biswas, K. M. Ho, C. M. Soukoulis, D. Turner, B. Vasiliu, S. C. Kothari, and Shawn Lin, Microwave Opt. Technol. Lett. **23**, 56 (1999).
[8] Alongkarn Chutinan and Susumu Noda, Appl. Phys. Lett. **75**, 3739 (1999).
[9] Jonathan P. Dowling, Michael Scalora, Mark J. Bloemer, and Charles M. Bowden, J. Appl. Phys. **75**, 1896 (1994).
[10] Sajeev John and Marian Florescu, J. Opt. A, Pure Appl. Opt. **3**, S103 (2001).
[11] A. Blanco *et al.*, Nature (London) **405**, 437 (2000).
[12] H. Miguez *et al.*, Chem. Commun. (Cambridge) **22**, 2736 (2002).
[13] M. Campbell *et al.*, Nature (London) **404**, 53 (2000).
[14] V. Berger, O. Gauthier-Lafaye, and E. Costard, J. Appl. Phys. **82**, 60 (1997).
[15] S. Shoji and S. Kawata, Appl. Phys. Lett. **76**, 2668 (2000).
[16] K. M. Ho, C. T. Chan, and C. M. Soukoulis, Phys. Rev. Lett. **65**, 3152 (1990).
[17] E. Yablonovitch, T. J. Gmitter, and K. M. Leung, Phys. Rev. Lett. **67**, 2295 (1991).
[18] C. C. Cheng and A. Scherer, J. Vac. Sci. Technol. B **13**, 2696 (1995).
[19] C. C. Cheng, A. Scherer, V. Arbet-Engels, and E. Yablonovitch, J. Vac. Sci. Technol. B **14**, 4110 (1996).
[20] G. Feiertag, W. Ehrfeld, H. Freimuth, H. Kolle, H. Lehr, M. Schmidt, M. M. Sigalas, C. M. Soukoulis, G. Kiriakidis, T. Pedersen *et al.*, Appl. Phys. Lett. **71**, 1441 (1997).
[21] C. Cuisin, A. Chelnokov, D. Decanini, D. Peyrade, Y. Chen, and J. m. Lourtioz, Opt. Quantum Electron. **34**, 13 (2002).

[22] A. Chelnokov, K. Wang, S. Rowson, P. Garoche, and J.-m. Lourtioz, Appl. Phys. Lett. **77**, 2943 (2000).
[23] J. Schilling, Rb. Wehrspohn, A. Birner, F. Müller, R. Hillebrand, U. Gosele, Sw. Leonard, Jp. Mondia, F. Genereux, Hm. van Driel *et al.*, J. Opt. A, Pure Appl. Opt. **3**, S121 (2001).
[24] M. Christophersen, J. Carstensen, A. Feuerhake, and H. Föll, Mater. Sci. Eng., B **69**, 194 (2000).
[25] Timothy Y. M. Chan and Sajeev John, Phys. Rev. E **68**, 046607 (2003).
[26] Ovidiu Toader, Mona Berciu, and Sajeev John, Phys. Rev. Lett. **90**, 233901 (2003).
[27] H. s. Sözüer and J. p. Dowling, J. Mod. Opt. **41**, 231 (1994).
[28] C. T. Chan, K. M. Ho, C. M. Soukoulis, R. Biswas, and M. Sigalas, Solid State Commun. **89**, 413 (1994).
[29] S. Y. Lin, J. G. Fleming, D. L. Hetherington, B. K. Smith, K. M. Ho, M. M. Sigalas, W. Zubrzycki, S. R. Kurtz, and Jim Bur, Nature (London) **394**, 251 (1998).
[30] J. G. Fleming and Shawn-Yu Lin, Opt. Lett. **24**, 49 (1999).
[31] S. Noda, K. Tomoda, N. Yamamoto, and A. Chutinan, Science **289**, 604 (2000).
[32] Kanna Aoki, Hideki T. Miyazaki, Hideki Hirayama, Kyoji Inoshita, Toshihiko Baba, Norio Shinya, and Yoshinobu Aoyagi, Appl. Phys. Lett. **81**, 3122 (2002).
[33] Michael C. Wanke, Olaf Lehmann, Kurt Müller, Qingzhe Wen, and Michael Stuke, Science **275**, 1284 (1996).
[34] Hong-Bo Sun, Shigeki Matsuo, and Hiroaki Misawa, Appl. Phys. Lett. **74**, 786 (1999).
[35] Brian H. Cumpston, Sundaravel P. Ananthavel, Stephen Barlow, Daniel L. Dyer, Jeffrey E. Ehrlich, Lael L. Erskine, Ahmed A. Heikal, Stephen M. Kuebler, I.-y. Sandy Lee, Dianne Mccord-Maughon *et al.*, Nature (London) **398**, 51 (1999).
[36] Scott R. Kennedy, Michael J. Brett, Ovidiu Toader, and Sajeev John, Nano Lett. **2**, 59 (2002).
[37] Ovidiu Toader and Sajeev John, Science **292**, 1133 (2001).
[38] Ovidiu Toader and Sajeev John, Phys. Rev. E **66**, 016610 (2002).
[39] Scott R. Kennedy, Michael J. Brett, Hernan Miguez, Ovidiu Toader, and Scott R. Kennedy, Photonics Nanostruct. Fundam. Appl. **1**, 37 (2003).
[40] H. S. Sözüer, J. W. Haus, and R. Inguva, Phys. Rev. B **45**, 13 962 (1992).
[41] N. A. Clark, A. J. Hurd, and B. J. Ackerson, Nature (London) **281**, 57 (1979).
[42] Pawel Pieranski, Contemp. Phys. **24**, 25 (1983).
[43] H. Míguez, A. Blanco, F. Meseguer, C. López, H. M. Yates, M. E. Pemble, V. Fornés, and A. Mifsud, Phys. Rev. B **59**, 1563 (1999).
[44] Yu. A. Vlasov, V. N. Astratov, A. V. Baryshev, A. A. Kaplyanskii, O. Z. Karimov, and M. F. Limonov, Phys. Rev. E **61**, 5784 (2000).
[45] Kurt Busch and Sajeev John, Phys. Rev. E **58**, 3896 (1998).
[46] Zhi-Yuan Li and Zhao-Qing Zhang, Phys. Rev. B **62**, 1516 (2000).
[47] Yu. V. Miklyaev *et al.*, Appl. Phys. Lett. **82**, 1284 (2003).
[48] I. Divliansky, T. S. Mayer, K. S. Holliday, and V. H. Crespi, Appl. Phys. Lett. **82**, 1667 (2003).
[49] X. Wang *et al.*, Appl. Phys. Lett. **82**, 2212 (2003).
[50] D. n. Sharp, M. Campbell, E. r. Dedman, M. t. Harrison, R. g. Denning, and A. j. Turberfield, Opt. Quantum Electron. **34**, 3 (2002).
[51] A. Feigel, Z. Kotler, and B. Sfez, Opt. Lett. **27**, 746 (2002).
[52] Shu Yang, Mischa Megens, Joanna Aizenberg, Pierre Wiltzius, Paul. M. Chaikin, and William B. Russel, Chem. Mater. **14**, 2831 (2002).
[53] Y. A. Vlasov, X.-Z. Bo, J. C. Sturm, and D. J. Norris, Nature (London) **414**, 289 (2001).
[54] Ivan B. Divliansky, Atsushi Shishido, Iam-Choon Khoo, Theresa S. Mayer, David Pena, Suzushi Nishimura, Christine D. Keating, and Thomas E. Mallouk, Appl. Phys. Lett. **79**, 3392 (2001).
[55] Atsushi Shishido, Ivan B. Diviliansky, I. C. Khoo, Theresa S. Mayer, Suzushi Nishimura, Gina L. Egan, and Thomas E. Mallouk, Appl. Phys. Lett. **79**, 3332 (2001).
[56] Chaitanya K. Ullal *et al.*, J. Opt. Soc. Am. A **20**, 948 (2003).
[57] A. Chelnokov, S. Rowson, J-m. Lourtioz, V. Berger, and J-y. Courtois, J. Opt. A, Pure Appl. Opt. **1**, L3 (1999).
[58] D. N. Sharp, A. J. Turberfield, and R. G. Denning, Phys. Rev. B **68**, 205102 (2003).
[59] Xianyu Ao and Sailing He, Opt. Express **12**, 978 (2004).
[60] L. Martín-Moreno, F. J. García-Vidal, and A. M. Somoza, Phys. Rev. Lett. **83**, 73 (1999).
[61] M. Maldovan *et al.*, Phys. Rev. B **65**, 165123 (2002).
[62] V. Babin, P. Garstecki, and R. Holyst, Phys. Rev. B **66**, 235120 (2002).
[63] Ovidiu Toader, Timothy Y. M. Chan, and Sajeev John, Phys. Rev. Lett. **92**, 043905 (2004).
[64] Martin Maldovan, Chaitanya K. Ullal, W. Craig Carter, and Edwin L. Thomas, Nat. Mater. **2**, 664 (2003).
[65] David Corne, Marco Dorigo, and Fred Glover, eds., *New Ideas in Optimization* (McGraw-Hill, New York, 1999), p. 79.
[66] K. Y. Lee *et al.*, J. Vac. Sci. Technol. B **13**, 3012 (1995).